Emil Vedvik

Spatial non-stationary models for pavement deterioration and traffic accidents

Master's thesis in Applied Physics and Mathematics
Supervisor: Ingelin Steinsland
June 2021

Master's thesis

NTNU
Norwegian University of
Science and Technology

Emil Vedvik

Spatial non-stationary models for pavement deterioration and traffic accidents

Master's thesis in Applied Physics and Mathematics
Supervisor: Ingelin Steinsland
June 2021

Norwegian University of Science and Technology
Faculty of Information Technology and Electrical Engineering
Department of Mathematical Sciences

NTNU
Norwegian University of
Science and Technology

Abstract

Effective pavement maintenance targeted at the right locations is important for retaining a high degree of road safety and maximizing the socioeconomic benefits from the resources allocated to maintenance activities. In cooperation with NTNU the Norwegian Public Road Administration target this problem, seeking methods for smarter maintenance.

In this thesis annual pavement surface measurements from 2016-2020 for E16 from Bergen to Voss are used to investigate the spatial dependencies between road segments in terms of the annual change in rut depth, i.e. *rutting*, in addition to a brief study on the occurrence of accidents. Various spatial models are proposed within a Bayesian framework, as latent Gaussian models, where spatial dependencies are included as Gaussian random fields (GRF). Spatial stationarity and non-stationarity varying with respect to the traffic intensity are considered for the rutting whereas non-stationarity varying with respect to curvature is considered for occurrence of accidents. The aim is two-fold, where the first is to learn about the physical nature of the spatial dependencies for these two responses, and if the road characteristics influence the spatial properties. Second, is the aim of capturing spatial variation constant in time, possibly highlighting locations with elevated rutting requiring a physical inspection, where a GRF model for rutting including a yearly spatial field and a spatial field constant in time is proposed and fitted.

The proposed models for rutting seems to work and provide insight into the physical nature of the spatial dependencies, with results indicating non-stationarity for rutting, with increasing standard deviation and decreasing spatial range of the GRF as the traffic intensity increases. Inclusion of a GRF constant in time is tractable from a maintenance and interpretation point of view, and seems to work well particularly at high traffic intensities, although the prior sensitivity is high. Assessing possible non-stationarity for the occurrence of accidents yields no clear results, and the proposed models are not able to distinguish between simulated data from a stationary and non-stationary process, which they did to some extent manage for the rutting models.

Sammendrag

Effektivt vedlikehold av vegdekker utført på egnede lokasjoner er viktig for å opprettholde en høy grad av trafikksikkerhet og maksimere den samfunnsøkonomiske nytten av midler satt av til vedlikeholdsaktiviteter. I samarbeid med NTNU sikter Statens Vegvesen seg inn mot denne problemstillingen, og søker metoder for smartere vedlikehold.

I denne oppgaven blir årlige målinger av tilstand på vegdekker mellom 2016-2020 for E16 mellom Bergen og Voss brukt til å undersøke romlige avhengigheter mellom vegsegmenter ved å se på årlig endring i spordybde, i.e. sporing, i tillegg til en kort studie av ulykkeshendelser. Ulike romlige modeller er foreslått innen et Bayesiansk rammeverk, i form av latente Gaussiske modeller, hvor romlige avhengigheter er inkludert som Gaussiske tilfeldige felt (GRF). Romlig stasjonæritet samt ikke-stasjonæritet som varierer med hensyn på trafikkmengde er vurdert for sporing, og romlig ikke-stasjonæritet som varierer med hensyn på horisontal kurvatur er vurdert for ulykkeshendelser. Målet med studien er tosidig, hvor det første er å lære mer om den fysiske naturen til de romlige avhengighetene for disse to responsene, og hvordan ulike vegkarakteristikker påvirker de romlige avhengighetene. Det andre målet omhandler å fange opp romlig variasjon konstant over tid, for å gi indikasjoner på lokasjoner med forhøyet mengde sporing og som krever en nøyere visuell inspeksjon, hvor en GRF modell for sporing som inkluderer et årlig romlig felt og et romlig felt konstant over tid er foreslått og tilpasset.

De foreslåtte modellene for sporing synes å virke og gir innsikt i den fysiske naturen til de romlige avhengighetene, med resultater som indikerer ikke-stasjonæritet for sporing, med en økning i standardavvik og reduksjon i den romlige rekkevidden for et GRF når trafikkmengden øker. Inkluderingen av et GRF konstant i tid viser nyttige egenskaper fra et vedlikeholdsperspektiv, med god tolkbarhet, og synes å virke bra spesielt ved høye trafikkmengder, dog er prior sensitiviteten høy. Mulig ikke-stasjonæritet for ulykkeshendelser gir ingen klare resultater, og de foreslåtte modellene er ikke i stand til å skille mellom simulerte data fra en romlig stasjonær- og ikke-stasjonær prosess, noe de foreslåtte modellene for sporing i større grad klarte.

Preface

This thesis is the result of the course *TMA4900 - Industrial Mathematics, Master's Thesis* at the Norwegian University of Science and Technology, concluding the Master of Science degree in Applied Physics and Mathematics. The work has been carried out during the spring of 2021, and is an extension of the preliminary project carried out during the fall of 2020.

I would like to thank my supervisor Ingelin Steinsland for her enthusiastic guidance, feedback and encouragement through the work of this thesis and the preliminary project. Further I would like to thank Dagfin Gryteselv and Siebert Doreen at the Norwegian Public Road Administration for their feedback and making the road measurement data available.

Finally, I would like to thank my family and friends, for all their support and encouragement.

<div align="right">

Emil Vedvik
Trondheim, June 2021

</div>

Contents

Chapter 1

Introduction

Maintaining a sufficient quality of the road pavement surface is of high importance for retaining safe driving conditions. A pavement surface in bad condition pose a serious threat for the traffic safety and increase the external stress acted upon vehicles. Following *Nullvisjonen* decided by the Norwegian Parliament in 2002, stating a vision that there should not be anyone killed or severely injured on Norwegian roads, there is a continuous effort made to make roads more suited to an increase in the total traffic, challenging weather conditions and dangerous surroundings. The Norwegian Public Roads Administration is responsible for this work and the Norwegian government (2016) has set a preliminary goal of a maximum of 350 killed and severely injured in 2030 to move in the right direction of achieving *Nullvisjonen*. Achieving the preliminary goal will need a substantial reduction compared to the annual averages the last five years with 751 killed and critical injured individuals (Statistics Norway, 2020).

Maintenance and prevention of pavement deterioration is a continuous process intertwined with the expansion of the road traffic network to an ever increasing traffic intensity and needs for more complex road structures, increasing the overall complexity of the road network. A more complex road network requires more maintenance and preventive measures, in which some locations and areas may lag behind as the complexity increases. Sund (2012, 2013) estimated the cost of eliminating the maintenance backlog on Norwegian state and county roads to 70-125 billion NOK, where around 40 percent are costs related to pavement and drainage. A solid pavement has an expected lifetime of 20-25 years, under ideal conditions, but average repaving frequencies in Norway is around 15 years (Aurstad et al., 2016) and even lower as the traffic intensity increases, observed average rutting were shown by Saba et al. (2006) to be increasing with respect to increasing traffic intensity. Although Bakløkk (2017) note that historically some of the deterioration at high traffic intensities is attributed to the use of studded tires, and the usage of such tires has declined in recent years, with the consequence that the repaving frequencies for roads with high traffic intensity have decreased slightly. The research project *SMARTer maintenance* initiated by the Norwegian Public Roads Administra-

tion (NPRA) in cooperation with the Norwegian University of Science and Technology is directed at improving and creating more efficient tools for maintenance and identifying locations at which maintenance or preventive measures are required, this thesis is written as a part of the research project.

No unique metric exist in terms of evaluating the overall condition of the pavement surface, considering the macroscopic properties of the surface, the rut depth, describing a depression in the surface formed by wheels, is commonly used to describe the condition. An elevated rut depth may be due to heavy traffic load, but also problems related to the sub base of the pavement or the subsoil. Ruts affect the steering abilities of a vehicle and prevent effective drainage, retaining water at the surface and leading to an increased risk of aquaplanning, in addition the presence of water further deteriorates the road.

The spatial variability of different pavement properties have been investigated by Lea and Harvey (2015a, 2015b), in general showing that correlation ranges might be far lower than pavement engineers might guess, with high spatial variability even within one area unit thought to be uniform. Svenson et al. (2016) employ a mixed proportional hazards model with a spatial random effect modelled as an intrinsic conditional autoregressive (ICAR) model to identify road segments needing maintenance, finding that spatial variation is present, but only explains around 17% of unexplained variation for the lifetime between road segments, and an estimated spatial range of 4 km for the lifetime of road segments. Using the ICAR model to include spatial effects are also found by Zhao et al. (2019) to be preferable, but only slightly, in terms of predicting the pavement deterioration, noting that the real gain from including spatial effects is the ability to estimate pavement deterioration when observations are missing, and the possibility to visualise regions with elevated deterioration.

In this thesis we consider the annual change in rut depth for road segments of 20 meter, with the objective of investigating the spatial dependencies along the road, specifically the nature of the spatial dependence structure. Following the framework introduced by Ingebrigtsen et al. (2014) and Ingebrigtsen et al. (2015) for including explanatory variables in the dependence structure of a Gaussian random field (GRF), we include spatial non-stationarity dependent on the traffic intensity at each road segment. Considering only spatial effects, among with different intercept terms, the spatial dependencies is the focus, and whether including different spatial fields can tell us something about the spatial nature of the change in rut depth and if this can highlight locations with elevated rutting and indicate where a physical inspection should be conducted. The inclusion of a GRF constant in time, proposed by Ingebrigtsen et al. (2015) for improving forecasting and interpolation of the spatial field for a precipitation process, and later used by Ødegård (2017) showed favourable results when a non-stationary spatial field which is constant in time is included. In this thesis the inclusion of such a field is motivated by the interpretation it has towards the rutting at different locations over time. The need for including

spatial non-stationarity has been questioned by Fuglstad et al. (2015), showing that non-stationary GRFs might not be needed to model non-stationary spatial data, and what specific type of non-stationarity being present need to be considered.

The spatial properties of road traffic accidents have been analysed and modelled for several decades, where modelling the spatial dependency between areal units and using spatial effects to account for unmeasured information are common approaches. Less attention has been given to geometrical features of the road in the last decades, possibly due to missing data or difficulties regarding data acquisition (Ziakopoulos & Yannis, 2020). Accounting for spatial effects in crash frequency analysis show an extensive use of conditional auto regressive (CAR) models (Ziakopoulos & Yannis, 2020), whereas modelling spatial dependencies with GRFs are not as widely applied in crash frequency analysis, although recent studies by Galgamuwa et al. (2021) incorporate spatial random effects with a GRF, and find it preferable over non-spatial models. Ziakopoulos and Yannis (2020) points to spatial modelling of micro-level road safety as one field within spatial crash frequency analyses given very little attention.

In the preliminary work of this thesis (Vedvik, 2020), one of the finding were that increasing the horizontal curvature of neighbouring road segments elevated the probability of accident. As a consequence we use the same models introduced for the change in rut depth and investigate if spatial dependencies regarding the occurrence of accidents may be attributed with non-stationarity controlled by the horizontal curvature of the road. The high number of road segments and low accident count lead to consider this through a Bernoulli likelihood, either accident or no accident, for each road segment.

The spatial dependence structure of the change in rut depth and occurrence of accidents are studied by considering the road E16 between the outskirts of Bergen and Voss. This constitutes a road of length 80 km, mainly in rural areas with a fair amount of changes in curvature. Historically this is a road very prone to accidents and one where great investments have and are to be made to increase the safety and conditions along the road. It is located in the western part of Norway, with a coastal climate and is among the locations with most annual precipitation in Norway. Water pose one of the biggest threats to the road in terms of flooding and in general reducing the lifetime of the road due to increased deterioration when water is present at the surface and subsoil of the road. This make it a suitable case study area for both the change in rut depth and occurrence of accidents. Annual road surface measurements aggregated every 20 meter are made available from NPRA, and we let each of these represent individual road segments, placing the approach taken in this thesis within a spatial micro-level domain for road safety, where the vast majority of previous studies have considered data aggregated for larger spatial units. The abundancy of road surface measurements make it feasible to consider small spatial units of 20 meter.

The proposed models are within a Bayesian framework, as latent Gaussian models (LGMs), a flexible subclass of Bayesian hierarchical models, where we have a latent field assumed to be Gaussian distributed. By assumption, a GRF can be included in the latent field, and the extensive use of GRFs in spatial modelling make LGMs applicable for modelling a wide range of spatial phenomena. The computational bottleneck of GRFs is overcome by creating a Gaussian Markov random field representation (GMRF) through the stochastic partial differential equation (SPDE) approach for GRFs with Matérn covariance function (Lindgren et al., 2011). The GMRF representation enables the use of the integrated nested Laplace approximation (INLA) for fast approximate Bayesian inference (Rue et al., 2009), a computational efficient alternative for LGMs compared to traditional simulation based techniques relying upon Markov chain Monte Carlo. The inference is carried out using the `R-INLA` package in `R`.

A note is to be made on the nomenclature used in the thesis, we consider annual changes in rut depth, and for practical reasons use the term rutting to describe this, e.g the phrase *rutting in 2016* describes the change in rut depth between 2015 and 2016. The pavement surface measurements are made in the summer months, so the aforementioned phrase really means the rut depth change between summer 2015 and summer 2016.

The thesis is organised in the following manner. The study area and data are introduced in Chapter 2, among with a brief exploration of the data. In Chapter 3 the relevant theory for latent Gaussian models, Gaussian random fields, INLA and SPDE approach are given. The models used for rutting and accidents, with their prior assumptions, are given in Chapter 4. The results from the rutting models are presented in Chapter 5, among with a prior sensitivity analysis and a simulation study. Brief results and a simulation study for the accident models are presented in Chapter 6, before closing the thesis with discussion, concluding remarks and suggestions for further work in Chapter 7.

Chapter 2

Study area and exploratory data analysis

In this chapter we present an introduction to the study area used in the case study, the relevant road measurements and a brief exploration of the data.

2.1 Study area and road measurements

Road measurements and accidents along the road E16 between the outskirts of Bergen and Voss are considered in the case study. This constitutes a total road length of 80 km, mainly in rural areas. The road is located in the western part of Norway, as displayed in Figure 2.1b, with a coastal climate and is among the locations with most annual precipitation in Norway. The actual road is shown in Figure 2.1a, with apparent proximity to fjords and mountains over a large proportion of the road.

2.1.1 Aggregation of road condition measurements

Road condition measurements for E16 in the years 2015-2020 have been made available by the courtesy of NPRA, where the road surface conditions are measured annually for the entire Norwegian road network. These observations consists of a large amount of road surface measurements, among them various geometry and structural metrics describing the overall condition of the road.

The data is gathered by ViaPPS, a measurement system developed by ViaTech in cooperation with NPRA. The system is mounted onto a vehicle, utilizing LiDAR technology to accurately measure the surface of the road and nearby surroundings. Measurements are made approximately every 8 centimetres of the road, given a driving velocity of 60 km/h of the vehicle conducting the measurements, the measurements are then aggregated and reported for every 20 meter. Each observation we consider represent aggregated data for 20 meter of road, from now on termed as a road segment, and we use the reported median values of the measurements within each road segment.
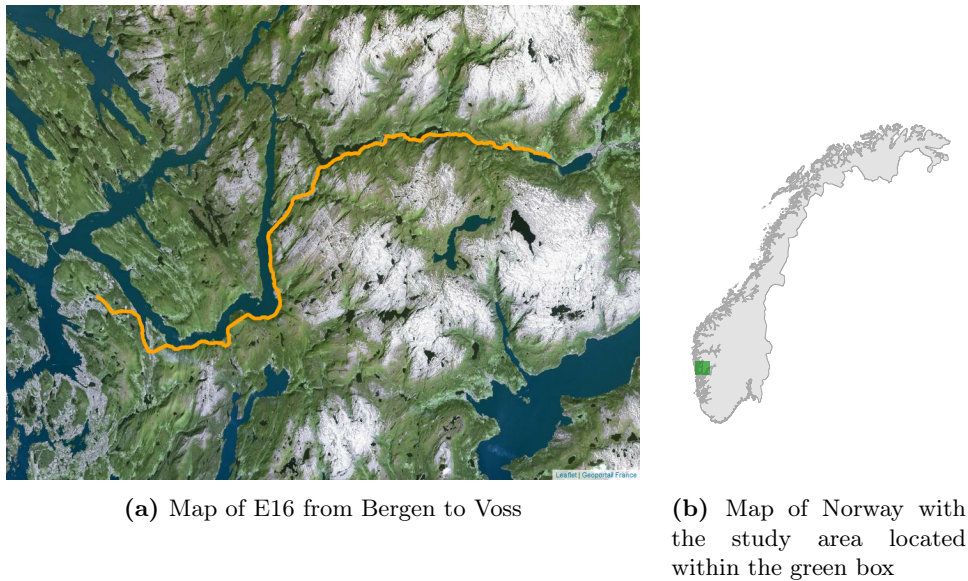
(a) Map of E16 from Bergen to Voss

(b) Map of Norway with the study area located within the green box

Figure 2.1: Location of the study area.

The annual measurements does not start at the exact same location every year, hence we treat the measurements for 2020 as the basis for creating the road segments, and use the geographical coordinates associated with the measurements for the previous years to find the most nearby road segment in the 2020 data set. If there are no errors in the registered locations the distance to the most nearby road section should not exceed 10 meters, thus a visual inspection is made for all cases where this occurs. This reveals that there are some small parts of the road that seems to have been altered and slightly moved during the study period, these measurements are included and is responsible for the high distances seen in Figure 2.2, but overall we find measurements from 2015-2019 very close to the road segments defined from the 2020 data. The measurements from 2015 and 2016 are incomplete, as seen from the annual number of road segments with valid measurements in Table 2.1. In addition the attempt to detect possible maintenance, introduced in Section 2.1.2, is not sufficiently accurate for the rutting in 2016, this combined with more than 30% missing measurements lead to omitting the rutting in 2016, and consider rutting for 2017-2020.

2.1.2 Rut depth

We consider the pavement deterioration in terms of the rut depth, and how this evolves over the period under study. Recall that the change in rut depth between two consecutive years is termed as the rutting and the rut depth is the actual depth of the rut in the given year. Let y_{ij} be the rutting and d_{ij} the rut depth for road segment i in year j. The road is subject to maintenance
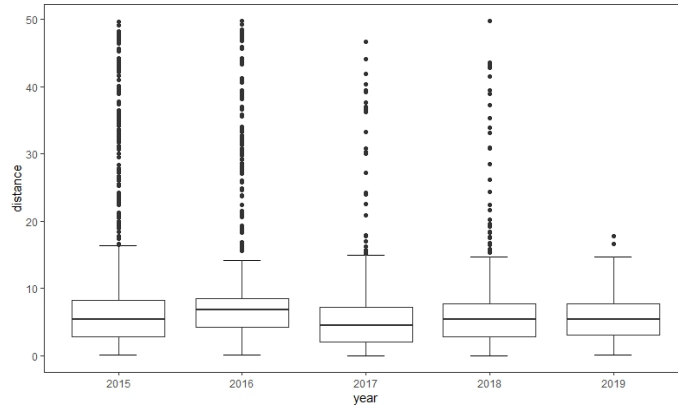
Figure 2.2: Distance between measurements 2015-2019 and the road segments defined by the measurements in 2020.

Table 2.1: Number of road segments with valid measurements and number of rural accidents.

Year	Measurements	Accidents
2015	2598	9
2016	2787	9
2017	4020	15
2018	4030	6
2019	4030	3
2020	4030	2

during the observation period and we see from Figure 2.3 that the rut depth for each road segment is slightly increasing, i.e. positive value for the rutting, until it suddenly decreases to a value equal or close to zero. We are interested in the deterioration of the road and do not want to capture the opposite process, maintenance. The measurements itself are highly accurate, but we showed that there are some error in the measurement locations within one road segment between different years. Because of this we cannot filter out maintenance solely based on whether the rutting in one particular year is negative or not, instead we filter this as

$$y_{ij} = \begin{cases} y_{ij}, & \text{if } y_{ij} \geq -d_{ij}/2, \\ \texttt{NaN}, & \text{if } y_{ij} < -d_{ij}/2. \end{cases}$$

If the rut depth has decreased, i.e. rutting, by at least $1/2$ of the actual rut depth, the rutting for the particular road segment that year is attributed as a missing observation. This results in including some values for rutting corresponding with negative values, with the source of error being this filtration and the location error for the road segments over consecutive years.

A more detailed view of the annual rut depth and rutting for a subset of the
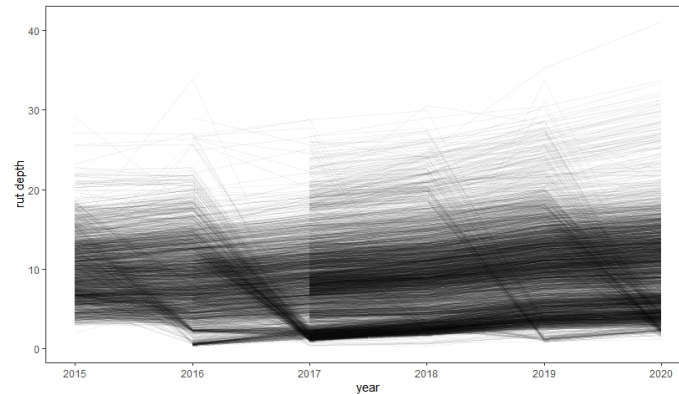
Figure 2.3: Rut depth for all road segments 2015-2020, each line represent the rut depth for one road segment.

road is shown in Figure 2.4, where the most notable trait of the rut depth for this part of the road is the decrease in rut depth for a large proportion of the road from 2019 to 2020, indicating that maintenance have been conducted. We also see that the filtering done to exclude maintenance seems to work in this particular case, as almost all of the rutting values at these road segments for 2020 are set as missing observations. We also observe that the annual rutting in general fluctuates around 0.5 and 2.0 mm, with some spikes at specific road segments.

2.1.3   Traffic intensity

The traffic intensity, measured in annual average daily traffic (AADT), is obtained through the publicly available data in the National Road Database (Statens Vegvesen, 2020). The traffic intensity is assumed to be constant in time, as the studied time period is limited. The traffic intensity is reported as 1000 meter stretches of road with the same intensity, and the traffic intensity for each 20 meter road segment is found by locating which of these stretches of intensity it is located within. The traffic load is the traditional way of incorporating the external stress caused by vehicles, taking into account the distribution of different vehicles and their loading. In this case the proportion of heavy vehicles is homogeneous along the road, thus the traffic load and the traffic intensity are proportional, and we consider the traffic intensity as an accurate measure of the traffic load.

2.2   Traffic accidents and curvature

Rural accidents in the period 2015-2020 is considered, that is accidents occurring along clean stretches of road with no nearby urban road structures, i.e. intersections, roundabouts, exit-ramps etc. We want to investigate how the ac-

(a) Rut depth in mm

(b) Rutting in mm
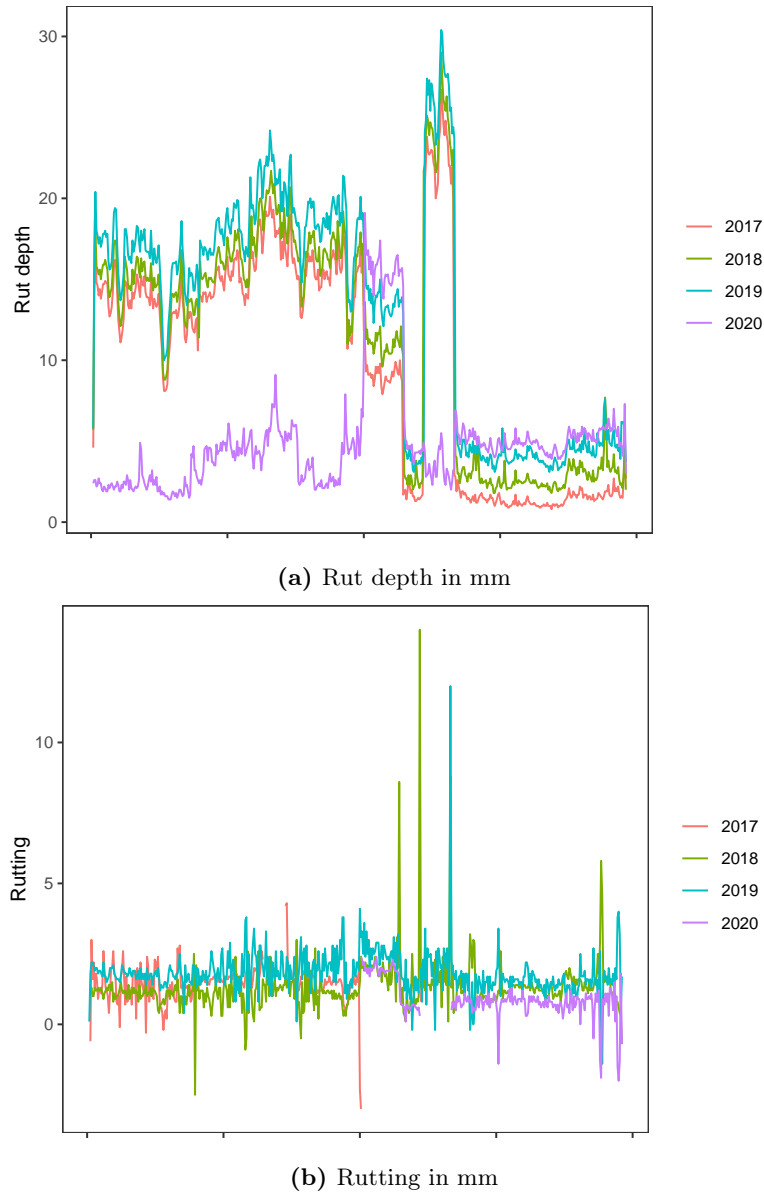
Figure 2.4: Annual rut depth and rutting for a subset of the road in a high traffic intensity area, constituting a total of 489 road segments.

cidents varies with curvature of the road, as found by Vedvik (2020), including urban accidents affects a spatial random effect, modelled by a GRF, to capture the clustering of accidents nearby urban road structures, thus urban accidents are excluded in this case.

As seen from Table 2.1 there are large annual variations in the number of accidents, but relative to the number of road segments this is low, hence we aggregate all the accidents in the period and record the observations as

accident/no accident for each road segment over the whole period 2015-2020.

The horizontal curvature is a geometrical metric of each road segment, measured as the radius of curvature, i.e. turning radius, with the curvature being the reciprocal of the radius of curvature. Consider a road segment with radius of curvature r, by combining the road segment multiple times into a full circle, this circle have a radius r, i.e. lowering the radius of curvature increases the actual curvature $c = 1/r$. The radius of curvature is measured as values $r \in (0 \text{ m}, 2000 \text{ m}]$, where 2000 m for practical purposes describes a road segment with no measurable curvature, thus the curvature has a range $c \in [1/2000, \infty)$. The curvature for the road segments are displayed in Figure 2.5, we see that almost half of the road segments corresponds to completely or almost straight stretches of road, the rest of the road segments are curved and there are a gradually decreasing number of segments for an increase in curvature.
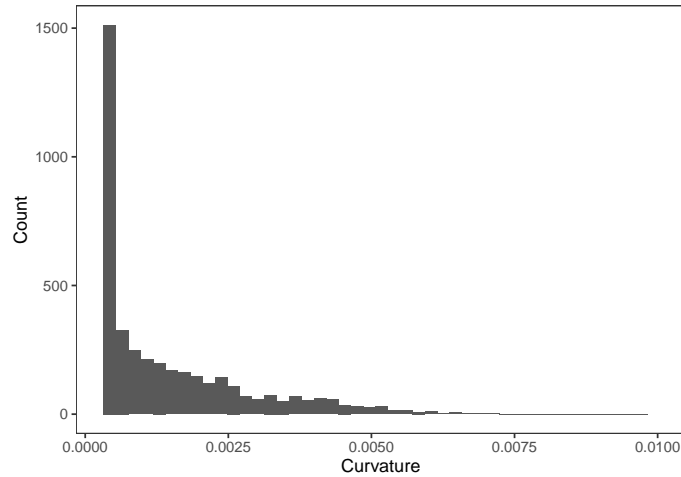
Figure 2.5: Curvature of the 4030 road segments.

2.3 Exploratory data analysis

The traffic intensity along the road is displayed in Figure 2.6, we see that the average annual daily traffic decreases as we move from west to east, with the largest fluctuations in AADT in the western part of the road, close to Bergen. The maximum value of 17 000 AADT is found at the westernmost road segments and the minimum value of 4500 AADT at the easternmost road segments.

The density estimates of the annual rutting after we have performed the filtering described in Section 2.1.2 are displayed in Figure 2.7. We see that the filtering seem to have excluded almost all of the maintenance activities, with only a small proportion of negative values for the rutting. The summary
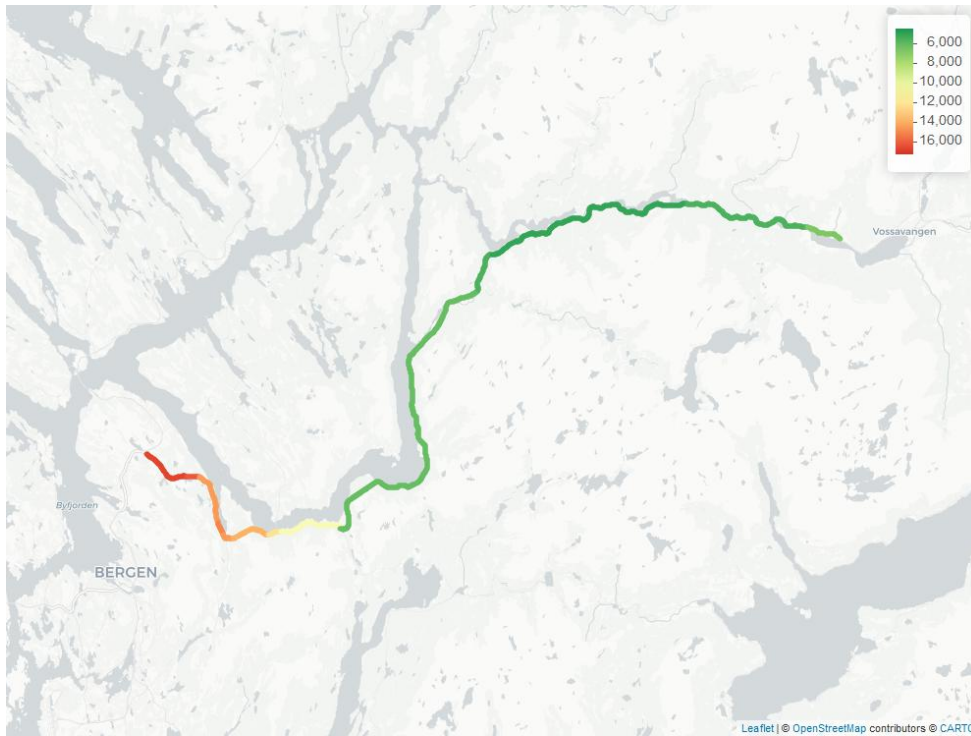
Figure 2.6: Annual average daily traffic along E16.

statistics in Table 2.2 shows more serious rutting in 2019 than the other years, with clearly higher mean and maximum values, the number of missing observations is fairly low for 2018-2020, but there are a large number of road segments with missing values for rutting in 2017, this is attributed to mostly the large amount of missing measurements in 2016, i.e. rutting for 2017 is not possible to calculate, and some values filtered as possible maintenance.

Table 2.2: Summary statistics of rutting for each year.

Year	Mean	Standard deviation	Minimum	Maximum	Missing observations
2017	1.14	1.05	-5.7	12.4	1777
2018	0.96	0.92	-3.3	14.0	72
2019	1.77	1.20	-4.5	28.5	117
2020	0.84	0.89	-5.8	11.8	347

Summary statistics for the rutting for four different traffic intensity groups are given by Table 2.3, the most notable trait is the high proportion of the road segments in the group with lowest traffic intensity. The mean rutting and standard deviation increases with increasing traffic intensity, but we also note a decrease as we move to the highest traffic intensity group.

The spatial variability of the annual rutting is displayed in the empirical
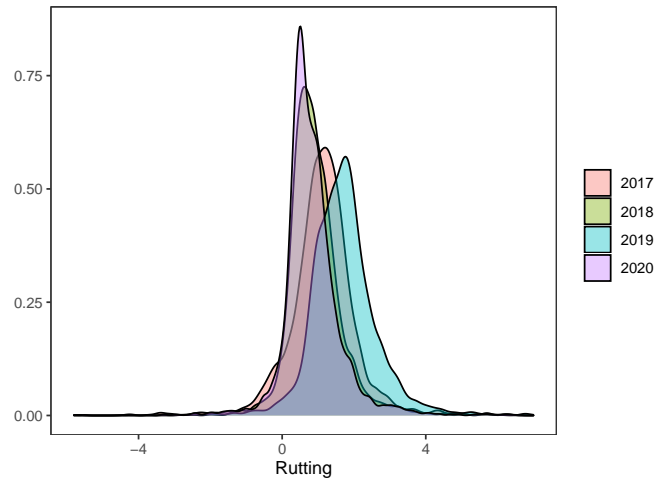
Figure 2.7: Density estimates of the rutting 2017-2020.

Table 2.3: Summary statistics of rutting grouped by traffic intensity, AADT.

AADT	Mean	Standard deviation	Segments
[4500, 7040]	0.84	1.08	3035
(7040, 12 100]	1.37	1.15	247
(12 100, 14 700]	1.54	1.43	200
(14 700, 17 200]	1.21	1.19	548

semivariograms in Figure 2.8. There is a clear tendency for all the variograms to level out at a short distance, in general around 400 meter, but 2019 has sudden spikes after 400 meter as well. The actual values of the semivariance between the years differ, this is partially explained by the density estimates in Figure 2.7, where 2019 have density estimates with higher variance than the other years, hence the semivariance attains higher values this year.

The location of the rural accidents in Figure 2.9 may indicate slightly more accidents in the western part of the road with higher traffic intensity, but considering that the traffic intensity in the west is more than threefold the intensity in the east, the effect of traffic intensity on the occurrences of accidents does not seem to be high.
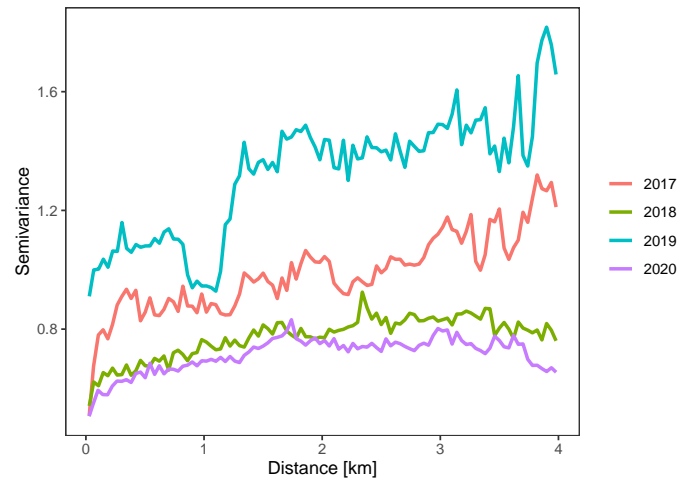
Figure 2.8: Variogram of the annual semivariance for rutting.
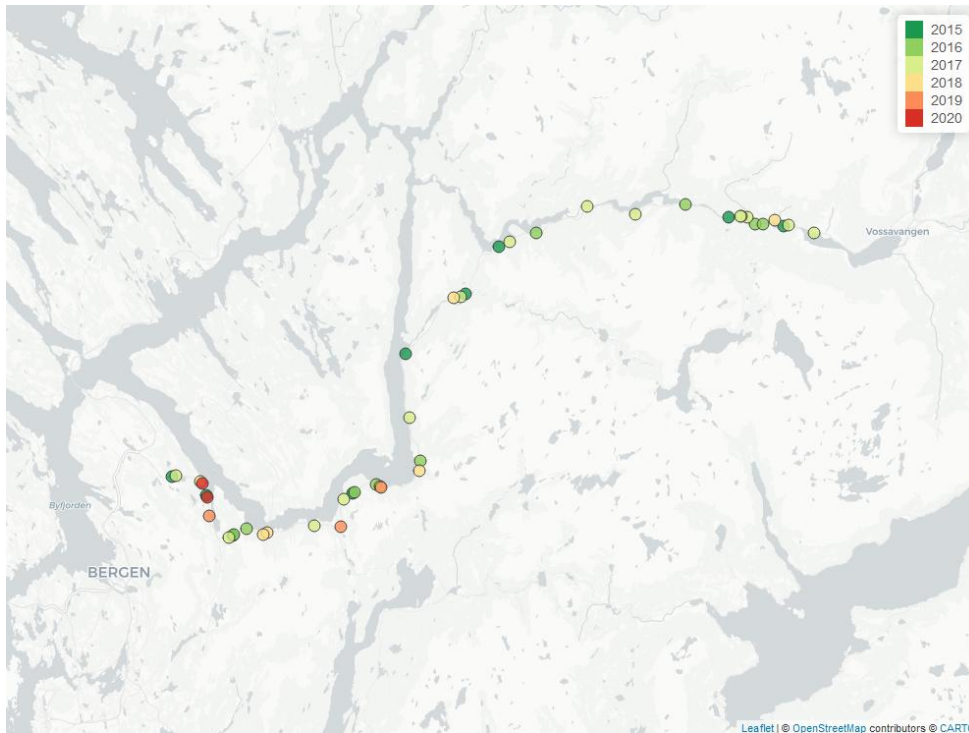
Figure 2.9: Location of rural accidents 2015-2020 along E16.

Chapter 3

Background

We introduce the necessary background and theory to describe our proposed models, how to do inference for the models and different model selection criterion. The main references are stated at the beginning of each section, and unless other references are given throughout the text, these are the referred source of each section.

3.1 Latent Gaussian model

We start by introducing the Latent Gaussian model (LGM), a particular subclass of the highly flexible Bayesian hierarchical model, following Blangiardo and Cameletti (2015) and Rue et al. (2009).

Bayesian inference is the process of updating prior beliefs upon observed data, opposed to the frequentist domain where model parameters are considered as unknown but fixed values, the Bayesian domain treats the model parameters as unknown random variables. The updating of the prior beliefs of the model parameters $\boldsymbol{x}$, given observed data $\boldsymbol{y}$, gives the posterior distribution of the model parameters, found from Bayes theorem as

$$p(\boldsymbol{x}|\boldsymbol{y}) = \frac{p(\boldsymbol{y}|\boldsymbol{x}) \times p(\boldsymbol{x})}{p(\boldsymbol{y})}. \tag{3.1}$$

The prior distribution $p(\boldsymbol{x})$ represents the prior belief, $p(\boldsymbol{y}|\boldsymbol{x})$ the likelihood function and $p(\boldsymbol{y})$ the marginal distribution of the data. By observing that the denominator is independent of $\boldsymbol{x}$ and considering this quantity as a normalizing constant, the posterior distribution is often specified as

$$p(\boldsymbol{x}|\boldsymbol{y}) \propto p(\boldsymbol{y}|\boldsymbol{x}) \times p(\boldsymbol{x}). \tag{3.2}$$

A Bayesian hierarchical model is often used in applications with several parameters defined on different levels, we now present a three-stage hierarchical model and introduce the term hyperparameters $\boldsymbol{\theta}$, that is parameters controlling the priors of the model parameters. A three-stage hierarchical model

consist of a likelihood function, a latent process and priors for the hyperparameters, stated as

$$\text{Stage 1:} \quad \boldsymbol{y}|\boldsymbol{x},\boldsymbol{\theta} \sim p(\boldsymbol{y}|\boldsymbol{x},\boldsymbol{\theta}), \tag{3.3a}$$

$$\text{Stage 2:} \quad \boldsymbol{x}|\boldsymbol{\theta} \sim p(\boldsymbol{x}|\boldsymbol{\theta}), \tag{3.3b}$$

$$\text{Stage 3:} \quad \boldsymbol{\theta} \sim p(\boldsymbol{\theta}). \tag{3.3c}$$

The latent Gaussian model arises when all the elements of the latent field $\boldsymbol{x}$ are assigned Gaussian priors. The mean μ_i of observation y_i is connected to a structured additive predictor η_i through an appropriate link function, $g(\mu_i) = \eta_i$, where the structured additive predictor takes the form

$$\eta_i = \beta_0 + \sum_{p=1}^{n_\beta} \beta_p x_{pi} + \sum_{j=1}^{n_f} f^{(j)}(u_{ji}) + \epsilon_i, \tag{3.4}$$

where β_0 is the intercept and β_p a linear effect of covariate $\boldsymbol{x}_p$. The terms $\{f^{(j)}(\cdot)\}$ are unknown functions of the covariates $\boldsymbol{u}$, used to model random effects. These may take several different forms, depending on the problem at hand, a collection of examples include smooth and nonlinear effects of the covariates, random intercept and slopes and temporal or spatial random effects. This yields a flexible model framework applicable to many different problems and models such as regression-, dynamic-, spatial- and spatiotemporal models.

All structured additive predictors and it's components are collected in the latent field, such that $\boldsymbol{x} = \{\beta_0, \boldsymbol{\beta}, \boldsymbol{\eta}, f^{(1)}(\cdot), f^{(2)}(\cdot), \dots\}$, and the observations $\boldsymbol{y}$ are assumed to be conditionally independent given the latent field and hyperparameters. The likelihood function for stage 1 in (3.3a) is now

$$p(\boldsymbol{y}|\boldsymbol{x},\boldsymbol{\theta}) = \prod_{i=1}^{n} p(y_i|x_i,\boldsymbol{\theta}), \tag{3.5}$$

where each observation y_i is dependent on only one element of the latent field.

Assuming a multivariate Normal prior of the latent field, with mean $\mathbf{0}$ and precision matrix $\mathbf{Q}(\boldsymbol{\theta})$, the latent process of stage 2 in (3.3b) is $\boldsymbol{x}|\boldsymbol{\theta} \sim \mathcal{N}\big(\mathbf{0}, \mathbf{Q}(\boldsymbol{\theta})^{-1}\big)$ with density

$$p(\boldsymbol{x}|\boldsymbol{\theta}) = (2\pi)^{-n/2} \big|\mathbf{Q}(\boldsymbol{\theta})\big|^{1/2} \exp\Big(-\frac{1}{2}\boldsymbol{x}'\mathbf{Q}(\boldsymbol{\theta})\boldsymbol{x}\Big), \tag{3.6}$$

where $|\cdot|$ is the matrix determinant and $'$ the transpose operator. Assuming that the elements of the latent Gaussian field are conditionally independent, yields a sparse precision matrix $\mathbf{Q}(\boldsymbol{\theta})$ such that (3.6) is a Gaussian Markov random field, introduced in Section 3.2.1. This specification gives rise to computational benefits to be utilized by the integrated nested Laplace approximation introduced in Section 3.3

The hyperparameters are assigned prior distributions in stage 3, and the Gaussian assumption of the latent field does not apply to these, they may be

assigned to any suitable prior distribution. The joint posterior distribution of the latent field and the hyperparameters, given the observations are found from (3.2) by using all three stages of the Bayesian hierarchical model (3.3), which yields

$$
\begin{aligned}
p(\boldsymbol{x}, \boldsymbol{\theta} | \boldsymbol{y}) &\propto p(\boldsymbol{\theta})\, p(\boldsymbol{x}|\boldsymbol{\theta})\, p(\boldsymbol{y}|\boldsymbol{x}, \boldsymbol{\theta}) \\
&\propto p(\boldsymbol{\theta}) \big|\mathbf{Q}(\boldsymbol{\theta})\big|^{1/2} \exp\left(-\frac{1}{2}\boldsymbol{x}'\mathbf{Q}(\boldsymbol{\theta})\boldsymbol{x} + \sum_{i=1}^{n} \log\big(p(y_i|x_i, \boldsymbol{\theta})\big)\right).
\end{aligned} \tag{3.7}
$$

3.2 Gaussian random fields

Data containing geographical information are collected and has applications within a vast area of disciplines. Spatial statistics governs a field within statistics where the random process assumed to be generating the data is considered a spatial random process, by taking the geographical information of the data into consideration.

We introduce the Gaussian random field, the associated covariance function, in particular the Matérn covariance function and Gaussian Markov random fields, based on Gelfand et al. (2010), Banerjee et al. (2004) and Rue and Held (2005).

Gaussian random fields (GRFs) are used extensively for spatial phenomena continuous in space, with convenient analytical properties and providing a good representation of the spatial phenomena in a wide range of applications (Lindgren et al., 2011). Consider a spatial domain $\mathcal{D} \subset \mathbb{R}^d$, the random field $\{Y(\boldsymbol{s}) : \boldsymbol{s} \in \mathcal{D}\}$ is a Gaussian random field if for any set of spatial locations $\{\boldsymbol{s}_1, \ldots, \boldsymbol{s}_n\}$ and all $n \in \mathbb{N}$

$$
\big(Y(\boldsymbol{s}_1), \ldots, Y(\boldsymbol{s}_n)\big) \sim \mathcal{N}(\boldsymbol{\mu}, \boldsymbol{\Sigma}), \tag{3.8}
$$

with mean vector $\boldsymbol{\mu} = \big(\mu(\boldsymbol{s}_1), \ldots, \mu(\boldsymbol{s}_n)\big)$ and covariance matrix $\boldsymbol{\Sigma}$ with elements $\Sigma_{ij} = \text{Cov}\big(Y(\boldsymbol{s}_i), Y(\boldsymbol{s}_j)\big) = C\big(Y(\boldsymbol{s}_i), Y(\boldsymbol{s}_j)\big)$, where $C(\cdot, \cdot)$ denotes the covariance function, and may be any positive definite function.

The GRF is said to be strictly stationary if the random field is invariant under spatial shifts, i.e. $\big(Y(\boldsymbol{s}_1), \ldots, Y(\boldsymbol{s}_n)\big)$ has the same distribution as $\big(Y(\boldsymbol{s}_1 + \boldsymbol{h}), \ldots, Y(\boldsymbol{s}_n + \boldsymbol{h})\big)$ for any $\boldsymbol{h} \in \mathbb{R}^d$. Second-order stationarity is a less restrictive condition, requiring that the mean vector is constant in space $\mu(\boldsymbol{s}_i) = \mu$ for any location $\boldsymbol{s}_i \in \mathcal{D}$, and that the covariance function does not depend on the location, only on the distance vector $(\boldsymbol{s}_i - \boldsymbol{s}_j)$, such that $\text{Cov}(\boldsymbol{s}_i, \boldsymbol{s}_j) = C(\boldsymbol{s}_i - \boldsymbol{s}_j)$. Strict stationarity implies second-ordrer stationarity, in general the converse is not true, but a special property of GRFs is that the converse statement is true and when we use the term stationary GRFs it is a reference to both strictly and second-order stationary GRFs. If the covariance function solely depend on the Euclidean distance between locations, and not the direction, the GRF and covariance function $\text{Cov}(\boldsymbol{s}_i, \boldsymbol{s}_j) = C(||\boldsymbol{s}_i - \boldsymbol{s}_j||)$ are said to be isotropic.

The dependence structure of a GRF is defined through the covariance function, several choices exists, although Stein (1999) makes a strong claim that the Matérn covariance function should be the preferred choice. Due to the Matérn covariance functions application in the SPDE approach for GRFs, introduced in Section 3.4, it is the covariance function considered in this study.

The covariance between the locations $\boldsymbol{s}_i, \boldsymbol{s}_j \in \mathcal{D}$ given by the isotropic Matérn covariance function is

$$C(\boldsymbol{s}_i, \boldsymbol{s}_j) = \frac{\sigma^2}{\Gamma(\nu)2^{\nu-1}} \left(\kappa||\boldsymbol{s}_i - \boldsymbol{s}_j||\right)^\nu K_\nu\left(\kappa||\boldsymbol{s}_i - \boldsymbol{s}_j||\right) \tag{3.9}$$

where $||\cdot||$ is the Euclidean distance, $\Gamma(\cdot)$ the gamma function, σ^2 the marginal variance and K_ν the modified Bessel function of second kind and order $\nu > 0$, with ν being the critical parameter measuring the smoothness. The constant $\kappa > 0$ is a scaling parameter related to the spatial range ρ, empirically derived to be

$$\rho = \frac{\sqrt{8\nu}}{\kappa} \tag{3.10}$$

with the interpretation that ρ is the distance at which the spatial correlation is close to 0.1, for $\nu \geq 0.5$ (Lindgren et al., 2011).

Aside from the tractable properties of GRFs, the covariance function in general give rise to dense covariance matrices $\boldsymbol{\Sigma}$, with a computational cost of $\mathcal{O}(n^3)$ in terms of factorizing dense $n \times n$ matrices, referred to as "the big n problem" of GRFs. Improving on the computational cost motivates the introduction of Gaussian Markov random fields.

3.2.1 Gaussian Markov random fields

Among the proposed workarounds of the computational bottleneck of GRFs, replacing the GRF with a Gaussian Markov random field (GMRF) is convenient and has several applications, notably in the SPDE approach for GRFs introduced in Section 3.4.

We introduce the notion of undirected graphs before the full definition of a GMRF. Consider a undirected graph $\mathcal{G} = (\mathcal{V}, \mathcal{E})$, where $\mathcal{V}$ is the set of vertices in the graph and $\mathcal{E}$ the set of edges $\{i, j\}$ where $i, j \in \mathcal{V}$ and $i \neq j$. There is an undirected edge between vertices i and j if, and only if, $\{i, j\} \in \mathcal{E}$, in the case where $\mathcal{V} = \{1, 2, \ldots, n\}$ the graph is said to be labelled.

The concept of conditional independence is important for understanding GMRFs, consider the random vector $\boldsymbol{Y} = (Y_1, \ldots, Y_n)$, the conditional independence between Y_i and Y_j are denoted as

$$Y_i \perp Y_j | \boldsymbol{Y}_{-ij},$$

where $\boldsymbol{Y}_{-ij}$ is all elements of $\boldsymbol{Y}$ except Y_i and Y_j. Conditional independence implies that the joint conditional distribution can be expressed as

$$p(Y_i, Y_j | \boldsymbol{Y}_{-ij}) = p(Y_i | \boldsymbol{Y}_{-ij})p(Y_j | \boldsymbol{Y}_{-ij}). \tag{3.11}$$

An important property of the precision matrix $\mathbf{Q} = \mathbf{\Sigma}^{-1} > 0$ of a Gaussian distributed random vector $\mathbf{Y}$ with mean $\boldsymbol{\mu}$ and covariance matrix $\mathbf{\Sigma}$, is that for $i \neq j$

$$Y_i \perp Y_j | \mathbf{Y}_{-ij} \iff Q_{ij} = 0. \tag{3.12}$$

Conditional independence between Y_i and Y_j may be read directly from the precision matrix, it also implies the reverse statement, if the conditional dependence structure between the elements of $\mathbf{Y}$ is known, we also know which elements of $\mathbf{Q}$ is nonzero.

The random vector $\mathbf{Y} \in \mathbb{R}^n$ is a GMRF with respect to a labelled graph $\mathcal{G} = (\mathcal{V}, \mathcal{E})$ with mean vector $\boldsymbol{\mu}$ and precision matrix $\mathbf{Q} > 0$ if the density is

$$p(\mathbf{Y}) = (2\pi)^{-n/2} |\mathbf{Q}|^{1/2} \exp\left(-\frac{1}{2}(\mathbf{Y} - \boldsymbol{\mu})'\mathbf{Q}(\mathbf{Y} - \boldsymbol{\mu})\right), \tag{3.13}$$

and

$$Q_{ij} \neq 0 \iff \{i, j\} \in \mathcal{E} \quad \text{for all} \quad i \neq j.$$

The computational efficiency of GMRFs is attained when the precision matrix is sufficiently sparse, by using sparse matrix algorithms for the factorization of the precision matrix the computational cost of a two-dimensional GMRF is in general $\mathcal{O}(n^{3/2})$.

3.3 Integrated nested Laplace approximation

Historically Bayesian inference has often relied upon simulation based techniques, such as Markov chain Monte Carlo (MCMC), with great flexibility but limitations related to computational efficiency as the model complexity increases. The integrated nested Laplace approximation (INLA), introduced by Rue et al. (2009), improves the computational efficiency for LGMs, with a deterministic algorithm for fast approximate Bayesian inference. Rather than focusing on the joint posterior distribution, INLA approximates the marginal posterior distributions of the parameters. The authors note that the approximation bias from INLA is less than the MCMC error when applied to typical examples from spatial statistics, that is, examples where the dimension of the latent Gaussian field is a few thousand, the posterior marginals are approximated by INLA in a couple of minutes, and a corresponding MCMC-sampler may need days to compute accurate results. Examples of LGMs shown to work well with INLA include generalized linear mixed models, stochastic volatility models, spatial and spatio-temporal models, with a wide area of applications (Martins et al., 2013).

We give an introduction to INLA based on Blangiardo and Cameletti (2015) and the original paper by Rue et al. (2009).

The latent Gaussian model and it's assumptions described in Section 3.1 is applicable with INLA if the latent field is a GMRF with density given by (3.13),

in addition there is the assumption that the dimension of the hyperparameter vector $\boldsymbol{\theta}$ should be kept small, typically 2-5 and not exceeding 20 (Rue et al., 2017). The joint posterior density of the latent field and hyperparameters in (3.7) is a high dimensional density and may be very difficult to interpret and approximate by simulation based techniques. The inferential approach with INLA focuses on approximating the posterior marginal densities $p(x_i|\boldsymbol{y})$ and $p(\theta_j|\boldsymbol{y})$, that is, an approximation to the integrals

$$p(x_i|\boldsymbol{y}) = \int \int p(\boldsymbol{x}, \boldsymbol{\theta}|\boldsymbol{y}) \, \mathrm{d}\boldsymbol{x}_{-i} \, \mathrm{d}\boldsymbol{\theta} = \int p(x_i|\boldsymbol{\theta}, \boldsymbol{y}) p(\boldsymbol{\theta}|\boldsymbol{y}) \, \mathrm{d}\boldsymbol{\theta} \tag{3.14}$$

$$p(\theta_j|\boldsymbol{y}) = \int \int p(\boldsymbol{x}, \boldsymbol{\theta}|\boldsymbol{y}) \, \mathrm{d}\boldsymbol{x} \, \mathrm{d}\boldsymbol{\theta}_{-j} = \int p(\boldsymbol{\theta}|\boldsymbol{y}) \, \mathrm{d}\boldsymbol{\theta}_{-j}, \tag{3.15}$$

where $\boldsymbol{\theta}_{-j}$ denotes all elements of $\boldsymbol{\theta}$ except θ_j. The core of the INLA methodology lies in building appropriate approximations to $p(\boldsymbol{\theta}|\boldsymbol{y})$ and $p(x_i|\boldsymbol{y}, \boldsymbol{\theta})$.

Starting with the joint posterior distribution of the hyperparameters, approximated as

$$p(\boldsymbol{\theta}|\boldsymbol{y}) = \frac{p(\boldsymbol{x}, \boldsymbol{\theta}|\boldsymbol{y})}{p(\boldsymbol{x}|\boldsymbol{\theta}, \boldsymbol{y})} \tag{3.16}$$

$$\propto \frac{p(\boldsymbol{y}|\boldsymbol{x}, \boldsymbol{\theta}) p(\boldsymbol{x}|\boldsymbol{\theta}) p(\boldsymbol{\theta})}{p(\boldsymbol{x}|\boldsymbol{\theta}, \boldsymbol{y})}$$

$$\approx \frac{p(\boldsymbol{y}|\boldsymbol{x}, \boldsymbol{\theta}) p(\boldsymbol{x}|\boldsymbol{\theta}) p(\boldsymbol{\theta})}{\tilde{p}(\boldsymbol{x}|\boldsymbol{\theta}, \boldsymbol{y})} \Bigg|_{\boldsymbol{x}=\boldsymbol{x}^*(\boldsymbol{\theta})} =: \tilde{p}(\boldsymbol{\theta}|\boldsymbol{y}), \tag{3.17}$$

where $\tilde{p}(\boldsymbol{x}|\boldsymbol{\theta}, \boldsymbol{y})$ is the Gaussian approximation of $p(\boldsymbol{x}|\boldsymbol{\theta}, \boldsymbol{y})$ given by Laplace's method (Appendix A), constructed by matching the mode $\boldsymbol{x}^*(\boldsymbol{\theta})$ and the curvature at the mode of $p(\boldsymbol{x}|\boldsymbol{\theta}, \boldsymbol{y})$. The Gaussian approximation is usually precise, as $p(\boldsymbol{x}|\boldsymbol{\theta}, \boldsymbol{y})$ is close to Gaussian, noted from the fact that it has a prior representation as a GMRF and the marginal distribution of $p(\boldsymbol{y})$ is usually well-behaved.

Finding $p(x_i|\boldsymbol{\theta}, \boldsymbol{y})$ is a slightly more complicated task, in general the dimension of $\boldsymbol{x}$ is far greater than $\boldsymbol{\theta}$, making it a more computationally expensive task. In the original paper by Rue et al. (2009) three approximations to $p(x_i|\boldsymbol{\theta}, \boldsymbol{y})$ are suggested, the Gaussian, the Laplace and a simplified Laplace approximation. The Gaussian is computationally effective, but generally not as accurate as the other, with possible errors in the location and lack of skewness (Rue & Martino, 2007), thus the focus is on the Laplace and simplified Laplace approximation.

By rewriting the latent field as $\boldsymbol{x} = (x_i, \boldsymbol{x}_{-i})$ and use the Laplace approx-

imation in a similar manner as in (3.17) we obtain

$$p\big(x_i|\boldsymbol{\theta},\boldsymbol{y}\big) = \frac{p\big((x_i,\boldsymbol{x}_{-i})|\boldsymbol{\theta},\boldsymbol{y}\big)}{p\big(\boldsymbol{x}_{-i}|x_i,\boldsymbol{\theta},\boldsymbol{y}\big)} \tag{3.18}$$

$$\propto \frac{p\big(\boldsymbol{x},\boldsymbol{\theta}|\boldsymbol{y}\big)}{p\big(\boldsymbol{x}_{-i}|x_i,\boldsymbol{\theta},\boldsymbol{y}\big)}$$

$$\approx \frac{p\big(\boldsymbol{x},\boldsymbol{\theta}|\boldsymbol{y}\big)}{\tilde{p}\big(\boldsymbol{x}_{-i}|x_i,\boldsymbol{\theta},\boldsymbol{y}\big)}\bigg|_{\boldsymbol{x}_{-i}=\boldsymbol{x}_{-i}^*(x_i,\boldsymbol{\theta})} =: \tilde{p}\big(x_i|\boldsymbol{\theta},\boldsymbol{y}\big), \tag{3.19}$$

where $\tilde{p}(\boldsymbol{x}_{-i}|x_i,\boldsymbol{\theta},\boldsymbol{y})$ is the Laplace Gaussian approximation to $p(\boldsymbol{x}_{-i}|x_i,\boldsymbol{\theta},\boldsymbol{y})$ and $\boldsymbol{x}_{-i}^*(x_i,\boldsymbol{\theta})$ its mode for given x_i and $\boldsymbol{\theta}$. The approximation is precise, but computationally expensive, as $\tilde{p}(\boldsymbol{x}_{-i}|x_i,\boldsymbol{\theta},\boldsymbol{y})$ must be recomputed for each value of x_i and $\boldsymbol{\theta}$.

The simplified Laplace approximation improves the computational efficiency while retaining a sufficiently accurate approximation in most cases, as this the default choice in `R-INLA` it is the one we will use. This approximation corrects the location and skewness errors of the Gaussian approximation by a Taylor's series expansion around the mode of the Laplace approximation $\tilde{p}(x_i|\boldsymbol{\theta},\boldsymbol{y})$. For a detailed description of this approximation the reader is referred to Rue et al. (2009).

The posterior marginals of interest in (3.14) and (3.15) are now approximated by

$$\tilde{p}(x_i|\boldsymbol{y}) = \int \tilde{p}(x_i|\boldsymbol{\theta},\boldsymbol{y})\tilde{p}(\boldsymbol{\theta}|\boldsymbol{y})\,\mathrm{d}\boldsymbol{\theta} \tag{3.20}$$

$$\tilde{p}(\theta_j|\boldsymbol{y}) = \int \tilde{p}(\boldsymbol{\theta}|\boldsymbol{y})\,\mathrm{d}\boldsymbol{\theta}_{-j}. \tag{3.21}$$

The integral in (3.20) is solved numerically by

$$\tilde{p}(x_i|\boldsymbol{y}) = \sum_k \tilde{p}(x_i|\boldsymbol{\theta}^{(k)},\boldsymbol{y})\tilde{p}(\boldsymbol{\theta}^{(k)}|\boldsymbol{y})\Delta_k, \tag{3.22}$$

where $\{\boldsymbol{\theta}^{(k)}\}$ is a set of integration points and $\{\Delta_k\}$ a set of corresponding weights. We close this section with a brief description of the numerical procedure used by INLA.

Note that the posterior marginals for the hyperparameters can be obtained directly from (3.21) by numerical integration, but this is computationally demanding, as we need to evaluate $\tilde{p}(\boldsymbol{\theta}|\boldsymbol{y})$ for a large number of configurations of $\boldsymbol{\theta}$. Instead $\tilde{p}(\boldsymbol{\theta}|\boldsymbol{y})$ is explored to find a suitable set of integration points $\{\boldsymbol{\theta}^{(k)}\}$ through the following steps

(i) Optimize $\log \tilde{p}(\boldsymbol{\theta}|\boldsymbol{y})$ with respect to $\boldsymbol{\theta}$ to locate the mode $\boldsymbol{\theta}^*$.
(ii) Compute the negative Hessian $\mathbf{H}$ at the modal configuration. Let $\boldsymbol{\Sigma} = \mathbf{H}^{-1}$, that is the covariance matrix of $\boldsymbol{\theta}$ if the density were Gaussian.

Compute the eigendecomposition $\boldsymbol{\Sigma} = \mathbf{V}\boldsymbol{\Lambda}^{1/2}\mathbf{V}'$ and define $\boldsymbol{\theta}$ via a new variable $\boldsymbol{z}$ such that

$$\boldsymbol{\theta}(\boldsymbol{z}) = \boldsymbol{\theta}^* + \mathbf{V}\boldsymbol{\Lambda}^{1/2}\boldsymbol{z}.$$

(iii) Using the $\boldsymbol{z}$-parameterization, a exploration scheme named the grid strategy builds a grid of points, where the bulk of the mass of $\tilde{p}(\boldsymbol{\theta}|)$ is located, but the computational cost grows exponentially with the number of hyperparameters. Rue et al. (2009) suggest the central composite design (CCD) strategy when the number of hyperparameters exceeds 4 to reduce computational costs, but it is suitable for fewer hyperparameters as well. Using the mode $\boldsymbol{\theta}^*$ and Hessian $\mathbf{H}$, suitable points in the reparameterized $\boldsymbol{\theta}$-space are selected for a second-order approximation of a response variable. The CCD strategy reduce the number of integration points, but is still able to capture the variability in the hyperparameter space.

The posterior marginals $\tilde{p}(\theta_j|\boldsymbol{y})$ are now computed by using an interpolation algorithm based on the values of $\tilde{p}(\boldsymbol{\theta}|\boldsymbol{y})$ evaluated in the set of integration points $\{\boldsymbol{\theta}_j^{(k)}\}$. The marginal posteriors $\tilde{p}(x_i|\boldsymbol{y})$ are computed by the numerical integration in (3.22) where the conditional posteriors $\tilde{p}(x_i|\boldsymbol{\theta}^{(k)}, \boldsymbol{y})$ are evaluated for every value in $\{\boldsymbol{\theta}^{(k)}\}$ on a grid of selected values for x_i.

For detailed descriptions of the numerical procedure the reader is referred to Rue et al. (2009) and Martins et al. (2013).

3.4 The stochastic partial differential equation approach

We give an introduction to the stochastic partial differential approach for stationary and non-stationary GRFs and how this enables inference for spatial modelling with GRFs using INLA, based on Lindgren et al. (2011), Blangiardo and Cameletti (2015) and Ingebrigtsen et al. (2014).

Spatial dependencies in the LGM framework are modelled by including spatial random effects in the structured additive predictor (3.4). Letting the spatial dependency be represented by a GRF is a convenient and common approach, but involves a huge computational cost, as this give rise to dense covariance matrices. As proposed by Lindgren et al. (2011) a GRF may be represented by a GMRF in the special case where the GRF has a Matérn covariance function, where the sparse covariance structure of the GMRF improves the computational efficiency, making it applicable with INLA.

The stochastic partial differential (SPDE) approach starts by noting that a GRF with Matérn covariance function is a weak stationary solution to the SPDE

$$\left(\kappa^2 - \Delta\right)^{\frac{\alpha}{2}}\left(\tau\xi(\boldsymbol{s})\right) = \mathcal{W}(\boldsymbol{s}), \quad \boldsymbol{s} \in \mathbb{R}^d, \tag{3.23}$$

where $\xi(\boldsymbol{s})$ is the GRF, $\mathcal{W}(\boldsymbol{s})$ is a Gaussian spatial white noise process, Δ the Laplacian, α a smoothing parameter, $\kappa > 0$ a scale parameter and τ a parameter controlling the variance. The explicit link between the SPDE in (3.23) and the Matérn parameters for the smoothness parameter ν and the marginal variance σ^2 is

$$\nu = \alpha - d/2 \tag{3.24}$$

$$\sigma^2 = \frac{\Gamma(\nu)}{\Gamma(\nu + d/2)(4\pi)^{d/2}\kappa^{2\nu}\tau^2}. \tag{3.25}$$

For the one dimensional case we have $d = 1$, and we fix $\alpha = 2$, as this is the default choice in `R-INLA`, hence $\nu = 3/2$, the empirically derived range parameter from (3.10) is now $\rho = 2\sqrt{3}/\kappa$. The marginal variance for this particular case is then $\sigma^2 = 1/4\kappa^3\tau^2$.

The solution to (3.23) is approximated by use of the finite element method with a basis function representation on a triangulation of the domain $\mathcal{D}$, stated as

$$\xi(\boldsymbol{s}) = \sum_{i=1}^{m} \phi_i(\boldsymbol{s})w_i, \tag{3.26}$$

with a set of basis functions $\{\phi_i\}$ and zero-mean Gaussian distributed weights $\{w_i\}$, where m is the total number of vertices in the triangulation. Lindgren et al. (2011) choose to use basis functions that are piecewise linear on each triangle, resulting in ϕ_i having value 1 at vertex i and 0 at all other vertices. The value of the field at vertex i is given by w_i, and values of the field in the interior of the triangles are determined by linear interpolation.

Obtaining the finite dimensional solution involves finding the distribution of the weights in (3.26) that fulfils (3.23). Let $\mathbf{Q}_{\alpha,\kappa^2}$ be the precision matrix for the weights $\boldsymbol{w}$, with $\alpha = 1, 2, \ldots$, as a function of the parameter κ in the SPDE (3.23). Using Neumann boundary conditions (zero normal derivative at the boundary of the domain $\mathcal{D}$), the precision matrices of the weights are

$$\begin{aligned}
\mathbf{Q}_{1,\kappa^2} &= \mathbf{K}_{\kappa^2}, \\
\mathbf{Q}_{2,\kappa^2} &= \mathbf{K}_{\kappa^2}\mathbf{C}^{-1}\mathbf{K}_{\kappa^2}, \\
\mathbf{Q}_{\alpha,\kappa^2} &= \mathbf{K}_{\kappa^2}\mathbf{C}^{-1}\mathbf{Q}_{\alpha-2,\kappa^2}\mathbf{C}^{-1}\mathbf{K}_{\kappa^2}, \qquad \text{for } \alpha = 3, 4, \ldots.
\end{aligned} \tag{3.27}$$

The $m \times m$ matrices $\mathbf{K}_{\kappa^2}, \mathbf{C}$ and $\mathbf{G}$ has elements

$$\begin{aligned}
\left(K_{\kappa^2}\right)_{ij} &= \kappa^2 C_{ij} + G_{ij}, \\
C_{ij} &= \langle \phi_i, \phi_j \rangle, \\
G_{ij} &= \langle \nabla\phi_i, \nabla\phi_j \rangle,
\end{aligned}$$

where $\langle \cdot, \cdot \rangle$ is the inner product and ∇ the gradient. Note that the matrix $\mathbf{C}^{-1}$ is dense, in turn making the precision matrix dense, thus the matrix $\boldsymbol{C}$ is replaced by a diagonal matrix $\tilde{\boldsymbol{C}}$, where $\tilde{C}_{ii} = \langle \phi_i, 1 \rangle$, making the precision matrix of the weights $\boldsymbol{w}$ sparse and a GMRF representation of $\boldsymbol{w}$ is obtained.

3.4.1 Non-stationarity

The SPDE approach for a stationary GRF can be extended to a non-stationary model, recall that the parameters κ and τ in the SPDE defined in (3.23) were constant in space. We introduce non-stationarity by letting the parameters depend on the spatial location $\boldsymbol{s}$, and rewrite the SPDE as

$$\left(\kappa(\boldsymbol{s})^2 - \Delta\right)^{\frac{\alpha}{2}}\left(\tau(\boldsymbol{s})\xi(\boldsymbol{s})\right) = \mathcal{W}(\boldsymbol{s}), \quad \boldsymbol{s} \in \mathbb{R}^d. \tag{3.28}$$

This specification make it possible to include non-stationarity through the SPDE parameters $\tau(\boldsymbol{s})$ and $\kappa(\boldsymbol{s})$ directly, without altering the covariance function of the GRF. The SPDE parameters itself can be described by a log-linear representation, as they tend to vary slowly with respect to the spatial location $\boldsymbol{s}$, given by

$$\log \tau(\boldsymbol{s}) = \theta_1^\tau + \sum_{k=2}^N b_k^\tau(\boldsymbol{s})\theta_k^\tau \tag{3.29}$$

$$\log \kappa(\boldsymbol{s}) = \theta_1^\kappa + \sum_{k=2}^N b_k^\kappa(\boldsymbol{s})\theta_k^\kappa, \tag{3.30}$$

where $\left\{b_k^{(\cdot)}\right\}$ are deterministic basis functions and the θ's are weight parameters. This specification introduce the possibility of including spatial explanatory variables in the dependence structure as basis functions.

The inclusion of space-dependent τ and κ only leads to minor changes in the GMRF representation of (3.28) from the one found in the stationary case. The precision matrix of the Gaussian weights $\boldsymbol{w}$ from (3.26) is a modified version of the stationary one, for $\alpha = 2$ we have

$$\mathbf{Q} = \mathbf{T}\left(\mathbf{K}^2\mathbf{C}\mathbf{K}^2 + \mathbf{K}^2\mathbf{G} + \mathbf{G}\mathbf{K}^2 + \mathbf{G}\mathbf{C}^{-1}\mathbf{G}\right)\mathbf{T}, \tag{3.31}$$

where $\mathbf{T}$ and $\mathbf{K}$ are diagonal $m \times m$ matrices with elements $T_{ii} = \tau(\boldsymbol{s}_i)$ and $K_{ii} = \kappa(\boldsymbol{s_i})$, again $\mathbf{C}$ need to be replaced with $\tilde{\mathbf{C}}$ in order for the Gaussian weights $\boldsymbol{w}$ to be a GMRF.

The explicit link between the SPDE and Matérn parameters from (3.24) and (3.25) are not valid in the non-stationary case. By disregarding the spatial interaction between the non-stationary parameter fields nominal approximations of the range and variance, for $\alpha = 2$ and $d = 1$, are

$$\rho(\boldsymbol{s}) \approx \frac{2\sqrt{3}}{\kappa(\boldsymbol{s})} \tag{3.32}$$

$$\sigma^2(\boldsymbol{s}) \approx \frac{1}{4\kappa(\boldsymbol{s})^3\tau(\boldsymbol{s})^2}. \tag{3.33}$$

Note that these approximations are valid for slowly varying $\kappa(\boldsymbol{s})$.

3.5 Model assessment

We have described the class of latent Gaussian models and how fast approximate Bayesian inference is obtained by the use of INLA. The flexibility of the latent Gaussian model framework allows for a wast combination of different models, thus we need to introduce some model selection criterion in order to compare different models. We introduce the deviance information criterion, conditional predictive ordinate, marginal likelihood and credible interval coverage.

3.5.1 Deviance information criterion

The deviance information criterion (DIC) proposed by Spiegelhalter et al. (2002) is a model selection criteria widely used for Bayesian models. It is composed of two terms, one quantifying the actual model fit and the second one the model complexity. The deviance of a model with likelihood $p(\boldsymbol{y}|\boldsymbol{\psi})$ is

$$\mathrm{D}(\boldsymbol{\psi}) = -\log\big(p(\boldsymbol{y}|\boldsymbol{\psi})\big), \tag{3.34}$$

where $\boldsymbol{\psi} = (\boldsymbol{x}, \boldsymbol{\theta})'$ in the LGM framework. The first term of DIC is the posterior expectation of the deviance $\bar{\mathrm{D}} = \mathrm{E}_{\boldsymbol{\psi}|\boldsymbol{y}}\big(\mathrm{D}(\boldsymbol{\psi})\big)$. The model complexity term is measured by

$$p_{\mathrm{D}} = \mathrm{E}_{\boldsymbol{\psi}|\boldsymbol{y}}\big(\mathrm{D}(\boldsymbol{\psi})\big) - \mathrm{D}\big(\mathrm{E}_{\boldsymbol{\psi}|\boldsymbol{y}}(\boldsymbol{\psi})\big) = \bar{\mathrm{D}} - \mathrm{D}(\bar{\boldsymbol{\psi}}), \tag{3.35}$$

denoted as the effective number of parameters, and the last term is the posterior mean of the parameters. The DIC is now given by

$$\mathrm{DIC} = \bar{\mathrm{D}} + p_{\mathrm{D}}, \tag{3.36}$$

where models with smaller DIC are better supported by the data.

3.5.2 Conditional predictive ordinate

The conditional predictive ordinate (CPO) (Pettit, 1990) is a diagnostic for Bayesian models, detecting surprising observations within a model. The CPO for one observation y_i is

$$\mathrm{CPO}_i = p(y_i|\boldsymbol{y}_{-i}),$$

that is, the CPO for each observation is the posterior probability of observing y_i from a model fit with all the other observations $\boldsymbol{y}_{-i}$. A small value indicate a poor fit of the model for observation y_i, and may be regarded as an outlier. The computation of CPO in INLA is found by solving

$$\mathrm{CPO}_i = \int p(y_i|\boldsymbol{y}_{-i}, \boldsymbol{\theta}) p(\boldsymbol{\theta}|\boldsymbol{y}_i) \, \mathrm{d}\boldsymbol{\theta},$$

and is in practise computed by numerical integration, further details are found in Held et al. (2010).

A summary measure of the CPO is calculated by

$$\text{CPO} = -\sum_{i=1}^{n} \log(\text{CPO}_i),$$

where smaller values indicate better fit.

3.5.3 Marginal likelihood

An approximation to the marginal likelihood is computed by INLA from the approximation of the joint posterior of the hyperparameters in (3.20) by marginalising with respect to $\boldsymbol{y}$ as

$$\tilde{p}(\boldsymbol{y}) = \int \frac{p(\boldsymbol{y}, \boldsymbol{x}, \boldsymbol{\theta})}{\tilde{p}(\boldsymbol{x}|\boldsymbol{\theta}, \boldsymbol{y})}\bigg|_{\boldsymbol{x}=\boldsymbol{x}^*(\boldsymbol{\theta})} \mathrm{d}\boldsymbol{\theta}. \tag{3.37}$$

The marginal likelihood is difficult to compute exactly and the approximation by INLA is shown to very accurate (Hubin & Storvik, 2016). We consider the logarithm of the marginal likelihood as a model selection criterion, where larger values indicate a better fit.

3.5.4 Credible interval coverage

Consider the $(1-\alpha)100\%$ credible interval $C_i = [\theta_i|\boldsymbol{y}_{1-\alpha/2}, \theta_i|\boldsymbol{y}_{\alpha/2}]$ for a parameter θ_i. Credible interval coverage, or only coverage, is a term we will refer to when we fix the parameters $\boldsymbol{\theta}^*$, simulate $\boldsymbol{y}^{(k)}$ from $p(\boldsymbol{y}|\boldsymbol{\theta}^*)$ and obtain new posterior estimates $\boldsymbol{\theta}^{(k)}|\boldsymbol{y}^{(k)}$. Repeating the procedure n times, we estimate the coverage of θ_i by

$$\text{coverage} = \frac{1}{n}\sum_{k=1}^{n} I(\theta_i^* \in C_i^{(k)}), \tag{3.38}$$

where $C_i^{(k)}$ is the credible interval for $\theta_i^{(k)}|\boldsymbol{y}^{(k)}$ and $I(\cdot)$ the indicator function

$$I(\theta_i^* \in C_i^{(k)}) = \begin{cases} 0 & \text{if } \theta_i^* \notin C_i^{(k)} \\ 1 & \text{if } \theta_i^* \in C_i^{(k)} \end{cases}$$

Chapter 4

Models and methods

We propose four different spatial models for the rutting, all within the LGM framework, with stationary and non-stationary GRFs. For the traffic accidents we propose two different models, with a stationary and non-stationary GRF. A brief overview of the prior specification for the model parameters and the triangulation used for the SPDE approach are also given.

We use the subscripts S and N-S to denote if the GRFs within each respective model are stationary or non-stationary, in addition the subscripts are used to discern between parameters from a model with stationary- and non-stationary GRF. When no subscript are given for the two GRFs we refer to the spatial fields in general, without any constraints on their stationary or non-stationary nature.

4.1 Latent Gaussian models for rutting

Consider the spatial domain of the road $\mathcal{D} \subset \mathrm{R}^1$, and a location s along the road $s \in \mathcal{D}$. Let the spatial process $\{\eta_j(s) : s \in \mathcal{D}\}$ describe the rutting along the road in year j. The rutting y_{ij} for road segment $i = 1, \ldots, n$ in year $j = 1, \ldots, T$ is given by the relation

$$y_{ij} = \eta_j(s_i) + \epsilon_{ij}, \tag{4.1}$$

where the measurement errors are assumed to be independent and identically distributed as $\epsilon_{ij} \sim \mathcal{N}(0, \tau_\epsilon^{-1})$. The rutting y_{ij} for segment i in year j is a discretized description for a 20 meter stretch of road, for the sake of simplicity each road segment is treated as a single point, not a line, in the modelling, where the midpoint of road segment i is set as the location s_i for the rutting y_{ij}.

The components included in the spatial process η_j are where we differ between the proposed models, for the sake of simplicity we include all fixed and random effects inside η_j, even though we termed this as the spatial process, the actual spatial effects are the elements in η_j described by a GRF.

The first model, Model I, for η_j, denoted with a subscript I, is one with a common intercept β, a year specific intercept γ_j and a GRF $\xi_j(s)$, given by

$$\eta_{j,\text{S,I}}(s) = \beta + \gamma_j + \xi_{j,\text{S}}(s),$$
$$\eta_{j,\text{N-S,I}}(s) = \beta + \gamma_j + \xi_{j,\text{N-S}}(s),$$

where the year specific intercepts are assumed to be independently and identically distributed as $(\gamma_1, \ldots, \gamma_T) \sim \mathcal{N}(\mathbf{0}, \tau_\gamma^{-1}\mathbf{I}_T)$. The spatial dependence is described by a GRF $\xi(s)$ with Matérn covariance function, where $\xi_j(s)$ for each $j = 1, \ldots, T$ are independent realisations, i.e. replicates, of $\xi(s)$. The GRF itself is described by a set of hyperparameters $\boldsymbol{\theta}$, to be specified in Section 4.1.1.

A second model is proposed, Model II, an extension of Model I, in addition to the annually varying spatial field $\xi(s)$, a spatial field which is constant in time $\omega(s)$ is included. The motivation for including this is to capture the spatial variation of the rutting that are constant over all years, we denote this field as one describing the spatial variation attributed from the pavement stress at different locations. The second model yields the following expressions for the stationary and non-stationary spatial process

$$\eta_{j,\text{S,II}}(s) = \beta + \xi_{j,\text{S}}(s) + \omega_{\text{S}}(s),$$
$$\eta_{j,\text{N-S,II}}(s) = \beta + \xi_{j,\text{N-S}}(s) + \omega_{\text{N-S}}(s).$$

As noted by Ingebrigtsen et al. (2015), the inclusion of $\omega(s)$ alters the interpretation of the annually varying GRF $\xi_j(s)$, to now describing the annual spatial deviation from the spatial field describing the pavement stress $\omega(s)$ and not the overall spatial variation, as is the case in model I.

The two models are closely related, but where Model I is mainly directed to target the actual spatial variation, Model II tries to distinguish between the spatial variation constant in time and the deviation from this observed for every year, where the field for the pavement stress $\omega(s)$ can possibly give indication of locations in the spatial domain $\mathcal{D}$ with elevated rutting over several years.

4.1.1 SPDE approach

The spatial dependencies in the propsed models are all GRFs with Matérn covariance function, making the SPDE approach for GRFs a tractable solution for including non-stationarity and reducing the computational cost. The SPDE approach involves constructing a triangulation of the spatial domain $\mathcal{D}$, onto which the basis function representation of the GRF is defined. We consider the same triangulation for the two GRFs $\xi(s)$ and $\omega(s)$ in both the stationary and non-stationary case. The spatial domain is one-dimensional, thus we can create a rather dense triangulation without compromising computational efficiency.

The chosen triangulation has a vertex every 60th meter, that is, each triangle covers three road segments, and we let the boundary extend 500 meter at each ends of the road. The spatial domain is one-dimensional, so possible boundary effects are considered to interfere with the results to a smaller extent than for two-dimensional problems, where not including vertices outside of the observation borders may cause the variance to be twice as large at the border as within the domain (Lindgren & Rue, 2015).

The basis function representation used by the finite element method in (3.26) for each of the GRFs is now

$$\xi_{j,\mathrm{S}}(s) = \sum_{k=1}^{m} \phi_k(s) v_{k,j,\mathrm{S}}, \qquad \xi_{j,\mathrm{N\text{-}S}}(s) = \sum_{k=1}^{m} \phi_k(s) v_{k,j,\mathrm{N\text{-}S}},$$

$$\omega_{\mathrm{S}}(s) = \sum_{k=1}^{m} \phi_k(s) w_{k,\mathrm{S}}, \qquad \omega_{\mathrm{N\text{-}S}}(s) = \sum_{k=1}^{m} \phi_k(s) w_{k,\mathrm{N\text{-}S}}.$$

Note that the Gaussian weights for $\xi_{j,\mathrm{S}}(s)$ and $\xi_{j,\mathrm{N\text{-}S}}(s)$ are dependent on j, a consequence of the assumption that they for each $j = 1,\dots,T$ are a independent realisation of the GRFs $\xi_{\mathrm{S}}(s)$ and $\xi_{\mathrm{N\text{-}S}}(s)$. However the basis functions $\{\phi_1,\dots,\phi_m\}$ are the same for all the GRFs, as the triangulation is the same. The GMRF representation is mapped from the triangulation vertices to the n observation locations by a projector matrix $\mathbf{A} \in \mathrm{R}^{n \times m}$, where each row of the projector matrix is given by $\mathbf{A}_i = \big(\phi_1(s_i),\dots,\phi_m(s_i)\big)$. The spatial process at each observation location s_i may now be denoted as

$$\eta_{j,\mathrm{S,I}}(s_i) = \beta + \gamma_j + \mathbf{A}_i \boldsymbol{v}_{j,\mathrm{S}}, \qquad \eta_{j,\mathrm{S,II}}(s_i) = \beta + \mathbf{A}_i(\boldsymbol{v}_{j,\mathrm{S}} + \boldsymbol{w}_{\mathrm{S}}),$$
$$\eta_{j,\mathrm{N\text{-}S,I}}(s_i) = \beta + \gamma_j + \mathbf{A}_i \boldsymbol{v}_{j,\mathrm{N\text{-}S}}, \qquad \eta_{j,\mathrm{N\text{-}S,II}}(s_i) = \beta + \mathbf{A}_i(\boldsymbol{v}_{j,\mathrm{N\text{-}S}} + \boldsymbol{w}_{\mathrm{N\text{-}S}}),$$

where $\boldsymbol{v}_j = (v_{1,j},\dots,v_{m,j})'$. Recall that these are zero mean Gaussian weights, with precision matrix given by (3.27) for $\boldsymbol{v}_{j,\mathrm{S}}$ and $\boldsymbol{w}_{\mathrm{S}}$, and (3.31) for $\boldsymbol{v}_{j,\mathrm{N\text{-}S}}$ and $\boldsymbol{w}_{\mathrm{N\text{-}S}}$

The hyperparameters controlling the dependence structure of the GRFs are given by the log-linear relations to the SPDE parameters $\tau(s)$ and $\kappa(s)$ in (3.29) and (3.30). For the stationary fields $\xi_{\mathrm{S}}(s)$ and $\omega_{\mathrm{S}}(s)$ these hyperparameters are $\boldsymbol{\theta}_{\mathrm{S}} = (\theta_{1,\tau}, \theta_{1,\kappa})'$, with the following relation to the SPDE parameters

$$\log \tau = \theta_{1,\tau},$$
$$\log \kappa = \theta_{1,\kappa}.$$

For the non-stationary fields $\xi_{\mathrm{N\text{-}S}}(s)$ and $\omega_{\mathrm{N\text{-}S}}(s)$ we introduce $f(s)$ in the dependence structure, that is the increase in traffic intensity at location s relative to the minimum observed traffic intensity. Let $g(s)$ be the actual traffic intensity, on the scale 10000 AADT, and

$$f(s) = g(s) - \min_{s \in \mathcal{D}} g(s),$$

such that $f(s) \in [0, \infty)$, this is done to ensure that the methodology for the prior specification of the SPDE parameters given by Ingebrigtsen et al. (2015) is applicable in this setting. The relation to the SPDE parameters is given by

$$\log \tau(s) = \theta_{1,\tau} + f(s)\theta_{f,\tau},$$
$$\log \kappa(s) = \theta_{1,\kappa} + f(s)\theta_{f,\kappa},$$

with hyperparameters $\boldsymbol{\theta}_{\text{N-S}} = (\theta_{1,\tau}, \theta_{f,\tau}, \theta_{1,\kappa}, \theta_{f,\kappa})'$. If $\theta_{f,\tau} = \theta_{f,\kappa} = 0$ we are back at the stationary model. For the sake of simplicity we will from now on use the term SPDE parameters to denote the hyperparameters $\boldsymbol{\theta}_{\text{S}}$ and $\boldsymbol{\theta}_{\text{N-S}}$ with a log-linear relation to the actual SPDE parameters τ and κ.

4.1.2   Priors

Let $\boldsymbol{x} = (\beta, \boldsymbol{\gamma}, \boldsymbol{v}, \boldsymbol{w})'$ denote the latent field, by assigning Gaussian priors to the elements of $\boldsymbol{x}$ we have a latent Gaussian field. The intercept is assigned a vague Gaussian prior, $\beta \sim \mathcal{N}(0, 1000)$, and the elements of $\boldsymbol{\gamma}$ were assumed to be independently and identically distributed as $\boldsymbol{\gamma} \sim \mathcal{N}(\mathbf{0}, \tau_\gamma^{-1}\mathbf{I}_T)$. The precision parameter τ_γ is a hyperparameter assigned a prior distribution $\tau_\gamma \sim \text{Gamma}(0, 5 \cdot 10^{-5})$, as we have no prior information about the parameter, and the same applies to the precision parameter of the measurement errors, $\tau_\epsilon \sim \text{Gamma}(0, 5 \cdot 10^{-5})$. Recall from Section 3.4 that the weights $\boldsymbol{v}$ and $\boldsymbol{w}$ are assumed to be zero-mean Gaussian, and the dependence structure of the GRFs are controlled by the SPDE parameters $\boldsymbol{\theta}_{\text{S}}$ and $\boldsymbol{\theta}_{\text{N-S}}$.

The priors for the SPDE parameters need to be set more carefully than the other hyperparameters, as they are shown to be prior sensitive and especially for $\boldsymbol{\theta}_{\text{N-S}}$ the priors should not be too informative (Ingebrigtsen et al., 2014). In addition there are no obvious physical interpretation of the parameters, further complicating the process of setting priors with some sense of prior information. We follow the procedure of Ingebrigtsen et al. (2015) for setting priors for the SPDE parameters, and introduce the approach in a similar manner. We will use the same priors for the stationary fields $\xi_{\text{S}}(s)$ and $\omega_{\text{S}}(s)$, and for the non-stationary fields $\xi_{\text{N-S}}(s)$ and $\omega_{\text{N-S}}(s)$.

Recall the relation between τ and κ from the SPDE in (3.23) and the marginal standard deviation

$$\sigma_S = \frac{1}{2\kappa^{3/2}\tau},$$

and the spatial range

$$\rho_S = \frac{2\sqrt{3}}{\kappa}.$$

By assigning informative priors to these parameters, which have a more clear physical interpretation, we get more informative priors for the SPDE parameters as well. Recall that $\log \tau = \theta_{1,\tau}$ and $\log \kappa = \theta_{1,\kappa}$, assume $\theta_\tau \sim (\mu_{1,\tau}, \sigma_{1,\tau}^2)$

and $\theta_\kappa \sim \mathcal{N}(\mu_{1,\kappa}, \sigma_{1,\kappa}^2)$. Properties of the log-normal distribution yields

$$\rho_{\mathrm{S}} \sim \log \mathcal{N}(\log 2\sqrt{3} - \mu_{1,\kappa}, \sigma_{1,\kappa}^2),$$

and

$$\sigma_{\mathrm{S}} \sim \log \mathcal{N}(-\log 2 - \mu_{1,\tau} - \mu_{1,\kappa}, \sigma_{1,\tau}^2 + \sigma_{1,\kappa}^2).$$

The quantile functions for the log-normal distributed spatial range and marginal standard deviation are

$$\rho_{\mathrm{S}}(p) = 2\sqrt{3} \exp(-\mu_{1,\kappa} + \sigma_{1,\kappa}\Phi^{-1}(p)),$$

and

$$\sigma_{\mathrm{S}}(p) = \frac{1}{2}\exp(-\mu_{1,\tau} - \mu_{1,\kappa} + \sqrt{\sigma_{1,\tau}^2 + \sigma_{1,\kappa}^2}\,\Phi^{-1}(p)),$$

where $0 \le p \le 1$ is a quantile, and $\Phi(\cdot)$ the cumulative distribution function for the standard normal distribution. By specifying two quantiles of ρ_{S} and σ_{S}, we get a set of four equations which can be solved for $\mu_{1,\tau}$, $\sigma_{1,\tau}^2$, $\mu_{1,\kappa}$ and $\sigma_{1,\kappa}^2$.

We consider values at the 0.5 and 0.9 quantile for the spatial range and marginal standard deviation. We saw from the variogram in Figure 2.8 that the spatial variability varied across different years, but relative to the size of the domain, 80 km, the spatial range seem to be several orders of magnitude lower. We set the 0.5 quantile to 400 m, and the 0.9 quantile to 1500 m, based on the findings in Section 2.3, and find $\mu_{1,\kappa} = -4.75$ and $\sigma_{1,\kappa}^2 = 1.06$. For the marginal standard deviation we find from the data reasonable values for the 0.5 quantile to be 0.6 mm and 0.9 quantile to 3 mm, this yields $\mu_{1,\tau} = 4.57$ and $\sigma_{1,\tau}^2 = 0.51$. This result in a rather narrow prior for $\theta_{1,\tau}$, but in the equations for $\mu_{1,\tau}$ and $\sigma_{1,\tau}^2$ they are dependent on each other, as well as $\mu_{1,\kappa}$ and $\sigma_{1,\kappa}^2$, and staying within sensible values for the 0.5 and 0.9 quantiles for the spatial range and standard deviation this are the best possible prior setting for $\theta_{1,\tau}$.

In the non-stationary case we rely on the nominal approximations in (3.32) and (3.33) for $\rho_{\mathrm{N\text{-}S}}(f)$ and $\sigma_{\mathrm{N\text{-}S}}(f)$, where $f = f(s)$ is the traffic intensity. Assigning Gaussian priors to $\boldsymbol{\theta}_{\mathrm{N\text{-}S}}$ and following the reasoning in the stationary case we have

$$\theta_{1,\tau} \sim \mathcal{N}(\mu_{1,\tau}, \sigma_{1,\tau}^2), \qquad \theta_{f,\tau} \sim \mathcal{N}(\mu_{f,\tau}, \sigma_{f,\tau}^2), \qquad (4.2)$$

$$\theta_{1,\kappa} \sim \mathcal{N}(\mu_{1,\kappa}, \sigma_{1,\kappa}^2), \qquad \theta_{f,\kappa} \sim \mathcal{N}(\mu_{f,\kappa}, \sigma_{f,\kappa}^2). \qquad (4.3)$$

Assuming independence of the θ's, the log-normal distributions of the nominal spatial range and standard deviation are now

$$\rho_{\mathrm{N\text{-}S}}(f) \sim \log \mathcal{N}(\log 2\sqrt{3} - \mu_{1,\kappa} - f\mu_{f,\kappa}, \sigma_{1,\kappa}^2 + f^2 \sigma_{f,\kappa}^2),$$

and

$$\sigma_{\mathrm{N\text{-}S}}(f) \sim \log \mathcal{N}(-\log 2 - \mu_{1,\tau} - \mu_{1,\kappa} - f(\mu_{f,\tau} + \mu_{f,\kappa}), \sigma_{1,\tau}^2 + \sigma_{1,\kappa}^2 + f^2(\sigma_{f,\tau}^2 + \sigma_{f,\kappa}^2)).$$

As these distributions change with the traffic intensity, a set of conditions is set up in order to make valid comparisons with the stationary prior distributions for the spatial range and marginal standard deviation:

1. $\rho_{\text{N-S}}(0) \overset{d}{=} \rho_{\text{S}}(0)$ and $\sigma_{\text{N-S}}(0) \overset{d}{=} \sigma_{\text{S}}(0)$
2. $\mu_{f,\tau} = \mu_{f,\kappa} = 0$
3. For a given reference traffic intensity f_0, c_ρ is the coefficient of variation for the ratio $\rho_{\text{N-S}}(f_0)/\rho_{\text{N-S}}(0)$ and c_σ the coefficient of variation for the ratio $\sigma_{\text{N-S}}(f_0)/\sigma_{\text{N-S}}(0)$

The first condition simply state that the stationary and non-stationary priors for the spatial range and standard deviation is equal at the lowest observed traffic intensity along the road. The second condition implies that the non-stationary spatial range and standard deviation has a prior assumption of no effect from a change in traffic intensity. The third condition let us control how much the priors are allowed to change as the traffic intensity changes, by specifying the coefficient of variation. This result in the following equations

$$\mu_{1,\tau,\text{S}} = \mu_{1,\tau,\text{N-S}}, \qquad \sigma^2_{1,\tau,\text{S}} = \sigma^2_{1,\tau,\text{N-S}},$$

$$\mu_{f,\tau} = 0, \qquad \sigma^2_{f,\tau} = \frac{1}{f_0^2} \log\left(\frac{c_\sigma^2 + 1}{c_\rho^2 + 1}\right),$$

$$\mu_{1,\kappa,\text{S}} = \mu_{1,\kappa,\text{N-S}}, \qquad \sigma^2_{1,\kappa,\text{S}} = \sigma^2_{1,\kappa,\text{N-S}},$$

$$\mu_{f,\kappa} = 0, \qquad \sigma^2_{f,\kappa} = \frac{1}{f_0^2} \log(c_\rho^2 + 1),$$

in order to ensure positive variance we need to require that $c_\sigma > c_\rho$. A more thorough evaluation of the coefficients of variation and the prior sensitivity is found in Ingebrigtsen et al. (2015).

We set the reference traffic intensity to $f_0 = 0.45$, corresponding to an actual traffic intensity of 9000 AADT, as $\min_{s \in \mathcal{D}} g(s) = 4500$. By setting $c_\rho = 0.9$ and $c_\sigma = 1.2$, we get $\sigma^2_{f,\tau} = 1.47$ and $\sigma^2_{f,\kappa} = 2.93$, with the priors $\theta_{f,\tau} \sim \mathcal{N}(0, 1.47)$ and $\theta_{f,\kappa} \sim \mathcal{N}(0, 2.93)$.

4.2 Latent Gaussian models for road accidents

We consider the same spatial domain $\mathcal{D} \subset \mathrm{R}^1$ as for the rutting models. The sparsity of accidents for each year along the road, as discussed in section 2.2, leads to omitting any temporal dependencies and consider all the accidents to be generated from one single realization of a spatial process. Now let the response variable of interest, y_i, be the binary outcome variable $\{0, 1\}$ denoting {no accident, accident} for road segment $i = 1, \ldots, n$, such that $y_i \sim \text{Bernoulli}(\pi_i)$, where $\pi_i = p(y_i = 1)$. This non-Gaussian response is fitted into the LGM framework with an appropriate link function $g(\cdot)$ such that $\eta_i = g(\pi_i) = g\big(\mathrm{E}(y_i)\big)$, with the logit link we have

$$\eta_i = \ln\left(\frac{\pi_i}{1 - \pi_i}\right) \iff \pi_i = \frac{\exp(\eta_i)}{1 + \exp(\eta_i)},$$

where η_i contains the elements of the latent Gaussian field.

Following Model I introduced for rutting we propose the inclusion of a stationary and non-stationary GRF with Matérn covariance function in η_i, among with a common intercept β, given as

$$\eta_i = \beta + \xi_{\mathrm{S}}(s_i),$$
$$\eta_i = \beta + \xi_{\mathrm{N\text{-}S}}(s_i).$$

Omitting the temporal dimension we are now left with only one single realization of the GRFs $\xi_S(s)$ and $\xi_{\mathrm{N\text{-}S}}(s)$.

4.2.1 SPDE approach

We follow the same configuration used for the GRFs for the rutting models, with the same triangulation of the domain. The basis function representation is now

$$\xi_{\mathrm{S}}(s) = \sum_{i=1}^{m} \phi_i(s) v_{i,\mathrm{S}},$$
$$\xi_{\mathrm{N\text{-}S}}(s) = \sum_{i=1}^{m} \phi_i(s) v_{i,\mathrm{N\text{-}S}}.$$

The log-linear relation to the SPDE parameters for the stationary GRF $\xi_{\mathrm{S}}(s)$ are

$$\log \tau = \theta_{1,\tau},$$
$$\log \kappa = \theta_{1,\kappa}.$$

The curvature at location s, given by $c(s)$ is introduced in the dependence structure for the non-stationary GRF $\xi_{\mathrm{N\text{-}S}}(s)$, with a log-linear relation to the

SPDE parameters as

$$\log \tau(s) = \theta_{1,\tau} + c(s)\theta_{c,\tau},$$
$$\log \kappa(s) = \theta_{1,\kappa} + c(s)\theta_{c,\kappa},$$

where the curvature $c(s)$ is scaled by a factor of 100, for the sake of avoiding computational issues in R-INLA, and we saw in Section 2.2 that the curvature mainly were under 0.01, such that the curvature values after scaling are still below 1.

4.2.2 Priors

Let the latent field be denoted by $\boldsymbol{x} = (\beta, \boldsymbol{v})'$, by assigning Gaussian priors to the elements of $\boldsymbol{x}$ the non-Gaussian likelihood is now fitted into the LGM framework. Similar to the priors used for the rutting models we let $\beta \sim \mathcal{N}(0, 1000)$, and the weights $\boldsymbol{v}$ are zero-mean Gaussian. The approach for assigning priors to the SPDE parameters as for the rutting models is difficult to apply now, as the sparsity of data make the prior assumptions regarding the spatial range and marginal standard deviation more difficult to assess. In addition the inclusion of a link function between the mean and the structured additive predictor where the GRF is contained, further complicate the interpretation, compared to the case with a Gaussian likelihood, thus we refrain from this approach.

We consider the SPDE parameters to be zero mean Gaussian, with variance 2.5 for $\theta_{1,\tau}$ and $\theta_{1,\kappa}$, and variance 1.5 for $\theta_{c,\tau}$ and $\theta_{c,\kappa}$. Then the two models are fitted to the data, and let $\hat{\theta}_{1,\tau,S}$ denote the marginal posterior mean of $\theta_{1,\tau}$ from fitting Model I_S. The marginal posterior means for all the SPDE parameters are used to refit Model I_S and I_{N-S} with new prior means, the priors for Model I_S is now

$$\theta_{1,\tau,S} = \mathcal{N}(\hat{\theta}_{1,\tau,S}, 2.5), \qquad \theta_{1,\kappa,S} = \mathcal{N}(\hat{\theta}_{1,\kappa,S}, 2.5),$$

and Model I_{N-S}

$$\theta_{1,\tau,N-S} = \mathcal{N}(\hat{\theta}_{1,\tau,N-S}, 2.5), \qquad \theta_{c,\tau} = \mathcal{N}(\hat{\theta}_{c,\tau}, 1.5),$$
$$\theta_{1,\kappa,N-S} = \mathcal{N}(\hat{\theta}_{1,\kappa,N-S}, 2.5), \qquad \theta_{c,\kappa} = \mathcal{N}(\hat{\theta}_{c,\kappa}, 1.5).$$

These are rather restrictive priors, as noted by Lindgren and Rue (2015), setting priors for these parameters is difficult, and letting the prior variance of $\theta_{c,\tau}$ and $\theta_{c,\kappa}$ become to large we run into numerical issues. Also Ingebrigtsen et al. (2014) encountered the same problems, noting that the optimisation procedure for finding the mode of $p(\boldsymbol{\theta}^*|\boldsymbol{y})$ fails if the priors of these parameters are to vague.

4.3 Simulation studies

In order to assess the models ability to separate between stationarity and non-stationarity we conduct a simulation study, where the purpose is to investigate

Model I_S and $I_{N\text{-}S}$'s ability to separate data generated from a stationary and non-stationary GRF. This is performed for both the rutting and accident models.

For the rutting models we keep the priors used for Model I_S and $I_{N\text{-}S}$ for the actual rutting data, described in Section 4.1.2. We consider four replicates from the GRF $\xi(s)$, and discard the year specific intercept term γ_j from $\eta_{j,S,I}(s)$ and $\eta_{j,N\text{-}S,I}(s)$. The parameter values $\beta_S, \beta_{N\text{-}S}, \tau_{\epsilon,S}, \tau_{\epsilon,N\text{-}S}, \boldsymbol{\theta}_S$ and $\boldsymbol{\theta}_{N\text{-}S}$ are fixed according to the marginal posterior means from fitting Model I_S and $I_{N\text{-}S}$ to the actual rutting data, presented in Table 5.1. The procedure for simulating a stationary and non-stationary data set for rutting, with 4 different observation years, and fitting models to the simulated observations, is described by Algorithm 1. Where $\mathbf{1}_{nT}$ is a vector of one's with nT elements.

Algorithm 1 Simulation study rutting

1: **procedure** SIMULATION RUTTING
2:     fix $\beta_S, \beta_{N\text{-}S}, \tau_{\epsilon,S}, \tau_{\epsilon,N\text{-}S}, \boldsymbol{\theta}_S$ and $\boldsymbol{\theta}_{N\text{-}S}$
3:     **repeat**
4:         sample $\boldsymbol{v}_S \sim \mathcal{N}(\mathbf{0}, \mathbf{Q}_S^{-1})$
5:         sample $\boldsymbol{v}_{N\text{-}S} \sim \mathcal{N}(\mathbf{0}, \mathbf{Q}_{N\text{-}S}^{-1})$
6:         sample $\boldsymbol{\epsilon}_S \sim \mathcal{N}(\mathbf{0}, \tau_{\epsilon,S}^{-1}\mathbf{I})$
7:         sample $\boldsymbol{\epsilon}_{N\text{-}S} \sim \mathcal{N}(\mathbf{0}, \tau_{\epsilon,N\text{-}S}^{-1}\mathbf{I})$
8:         calculate stationary sample $\boldsymbol{y}_S = \beta_S\mathbf{1}_{nT} + \mathbf{A}\boldsymbol{v}_S + \boldsymbol{\epsilon}_S$
9:         calculate non-stationary sample $\boldsymbol{y}_{N\text{-}S} = \beta_{N\text{-}S}\mathbf{1}_{nT} + \mathbf{A}\boldsymbol{v}_{N\text{-}S} + \boldsymbol{\epsilon}_{N\text{-}S}$
10:       fit Model I_S and $I_{N\text{-}S}$ to $\boldsymbol{y}_S$
11:       fit Model I_S and $I_{N\text{-}S}$ to $\boldsymbol{y}_{N\text{-}S}$
12:     **until** 100 repetitions
13: **end procedure**

For the accident models we keep the priors given in Section 4.2.2 for Model I_S and $I_{N\text{-}S}$. Fixing the parameter values $\beta = -4$, $\theta_{1,\tau} = 8$ and $\theta_{1,\kappa} = -5$ in the stationary case, and include $\theta_{c,\tau} = -5$ and $\theta_{c,\kappa} = 2$ in the non-stationary case, i.e. $\beta, \theta_{1,\tau}$ and $\theta_{1,\kappa}$ are equal in both the stationary and non-stationary case. The full procedure is given in Algorithm 2, where $logit^{-1}(\eta_i) = \exp(\eta_i)/(1 + \exp(\eta_i))$ denotes the inverse logit link function.

4.4   Inference and software

The proposed models for rutting and accidents fit into the LGM framework, as we assume all elements of the latent field $\boldsymbol{x}$ to have Gaussian priors, in addition the spatial effects are modelled through GRFs, and using the SPDE approach we obtain GMRF representations of the GRFs making the models applicable with INLA, for fast approximate Bayesian inference. All data analysis and model fitting are performed by the use of the statistical computing tool R (R Development Core Team, 2008) and the implementation of INLA in the

---

Algorithm 2 Simulation study accidents

1: **procedure** SIMULATION ACCIDENTS
2:     fix $\beta_S, \beta_{N\text{-}S}, \boldsymbol{\theta}_S$ and $\boldsymbol{\theta}_{N\text{-}S}$
3:     **repeat**
4:         sample $\boldsymbol{v}_S \sim \mathcal{N}(\mathbf{0}, \mathbf{Q}_S^{-1})$
5:         sample $\boldsymbol{v}_{N\text{-}S} \sim \mathcal{N}(\mathbf{0}, \mathbf{Q}_{N\text{-}S}^{-1})$
6:         calculate $\boldsymbol{\eta}_S = \beta_S \mathbf{1}_n + \mathbf{A} \boldsymbol{v}_S$
7:         calculate $\boldsymbol{\eta}_{N\text{-}S} = \beta_{N\text{-}S} \mathbf{1}_n + \mathbf{A} \boldsymbol{v}_{N\text{-}S}$
8:         calculate $\pi_{i,S} = logit^{-1}(\eta_{i,S})$, $\boldsymbol{\pi}_S = (\pi_{i,S}, \ldots, \pi_{n,S})'$
9:         calculate $\pi_{i,N\text{-}S} = logit^{-1}(\eta_{i,N\text{-}S})$, $\boldsymbol{\pi}_{N\text{-}S} = (\pi_{i,N\text{-}S}, \ldots, \pi_{n,N\text{-}S})'$
10:         sample stationary accidents $\boldsymbol{y}_S \sim$ Bernoulli$(\boldsymbol{\pi}_S)$
11:         sample non-stationary accidents $\boldsymbol{y}_{N\text{-}S} \sim$ Bernoulli$(\boldsymbol{\pi}_{N\text{-}S})$
12:         fit Model I_S and $I_{N\text{-}S}$ to $\boldsymbol{y}_S$
13:         fit Model I_S and $I_{N\text{-}S}$ to $\boldsymbol{y}_{N\text{-}S}$
14:     **until** 100 repetitions
15: **end procedure**

---

package `R-INLA` (Rue et al., 2009) is used for fast inference for all the proposed LGMs.

The spatial properties of the data used for finding the distance between annual road measurements are handled by the use of the `sf` package (Pebesma, 2018). Plotting are performed by the `ggplot2` package (Wickham, 2016), except for the different maps, these are generated by use of the `mapview` package, to generate high resolution maps for small spatial domains.

Chapter 5

Results: Rutting

In this chapter we fit the models introduced in Section 4.1 to the rutting in 2017-2020, that is, in total four models, a stationary and non-stationary model within each of the proposed models, Model I and II. The models are compared in terms of their fit to the data, the interpretation of the potential underlying process driving the change in rutting and their usability from a maintenance planning perspective.

The models' ability to separate data generated from a spatial stationary and non-stationary process are investigated in a simulation study. In addition to an investigation of how the approach for setting informative priors for the SPDE parameters fares compared to a more naive non-informative approach.

The subscript ξ and ω are used for the SPDE parameters from Model II to reference which GRF they are contained within.

5.1 Case study

We start of by presenting results from model I, in particular the estimates for the SPDE parameters and the implication for the spatial dependency structure. We also look at how the results differ between the different years, by fitting the model to only a single year at a time, for each year 2017-2020. We continue by presenting results from Model II, and compare the results with Model I, upon which it is based, but with a more complex structure. The models ability to fit to the data is evaluated by DIC, CPO and the marginal likelihood. The prior distributions are as described in Section 4.1.2, recall that we use the same priors for the SPDE parameters for both fields $\xi(s)$ and $\omega(s)$ in Model II.

5.1.1 Model fit

The estimated parameters and 95% credible interval from the stationary and non-stationary model I fitted to data 2017-2020 are displayed in Table 5.1. The intercept term β shows no obvious deviations between the stationary and non-stationary case, we observe the same for the precision τ_ϵ of the error term ϵ, with

$\tau_{\epsilon,\text{S}}$ slightly lower than $\tau_{\epsilon,\text{N-S}}$, indicating that the error term in the stationary model explains more of the overall variability than in the non-stationary model. The precision τ_γ for the random intercept term for the different years show the same pattern, with slightly lower estimated precision for the stationary model. We also note that the credible intervals for both $\tau_{\gamma,S}$ and $\tau_{\gamma,\text{N-S}}$ is very wide, hence the estimated precision is quite uncertain, although neither of the credible intervals contain zero, so there seems to be significant differences between the years.

Continuing with the SPDE parameters we see that the parameters $\theta_{1,\tau,\text{S}}$ and $\theta_{1,\tau,\text{N-S}}$ are fairly similar, both of the estimated parameters are contained in the other ones credible interval, and neither contain zero. We observe a larger deviation between the estimate for the parameters $\theta_{1,\kappa,\text{S}}$ and $\theta_{1,\kappa,\text{N-S}}$, where both estimated parameters are barely contained within the others credible interval. Moving on the the SPDE parameters controlling the non-stationarity of the GRF $\xi_{\text{N-S}}(s)$, we see that the credible intervals for both $\theta_{f,\tau}$ and $\theta_{f,\kappa}$ does not contain zero, rather far from it, indicating that non-stationarity controlled by the traffic intensity might be reasonable.

Table 5.1: Posterior mean and 95% credible interval of the hyperparameters and fixed effect, from stationary and non-stationary model I fitted to rutting 2017-2020.

	Model	mean I_S	$I_{\text{N-S}}$	95% CI I_S	$I_{\text{N-S}}$
β		1.18	1.24	(0.79, 1.56)	(0.92, 1.56)
$\theta_{1,\tau}$		6.94	6.63	(6.56, 7.24)	(6.13, 7.00)
$\theta_{1,\kappa}$		-4.74	-4.53	(-4.93, -4.50)	(-4.76, -4.23)
$\theta_{f,\tau}$			-3.27		(-3.62, -2.92)
$\theta_{f,\kappa}$			1.84		(1.64, 2.04)
τ_γ		9.95	10.80	(2.05, 26.94)	(2.26, 29.05)
τ_ϵ		1.42	1.58	(1.38, 1.47)	(1.53, 1.64)

The interpretation of the estimated SPDE parameters are displayed in Figure 5.1, where the spatial range and standard deviation is attained by using the relations in (3.10) and (3.25), and the nominal approximations in the non-stationary case from (3.32) and (3.33). The posterior mean of the range is 396 m in the stationary model, the implication of the posterior marginal mean of $\theta_{1,\kappa,\text{N-S}}$ being higher than $\theta_{1,\kappa,\text{S}}$ is now clear, as the range for the non-stationary model is below 396 m even at the base level traffic intensity, and decrease as the traffic intensity increases. The non-stationary range show a steep decrease, and for the maximum observed traffic intensity of 17 000 AADT, it is only 31 m, indicating that road segments being second neighbours (40 meters apart) are practically uncorrelated. We should note that only about 25% of the road has a traffic intensity exceeding 10 000 AADT, and we might see signs of overfitting to the small proportion of the road with high traffic intensity, and

further extrapolating to higher traffic intensities than 17 000 AADT lead to a range where each road segment is uncorrelated to it's closest neighbour as well. The standard deviation in the stationary case is 0.63 mm, and for the non-stationary 0.625 mm at the base level, increasing as the traffic intensity increases. We observe that the standard deviation of the field, given as dots, show the same tendency, although for a given traffic intensity their deviation is rather large, and the standard deviation in the non-stationary case seems to follow the maximum observed standard deviations, possibly indicating a too strong dependency on the traffic intensity.

(a) Range

(b) Standard deviation
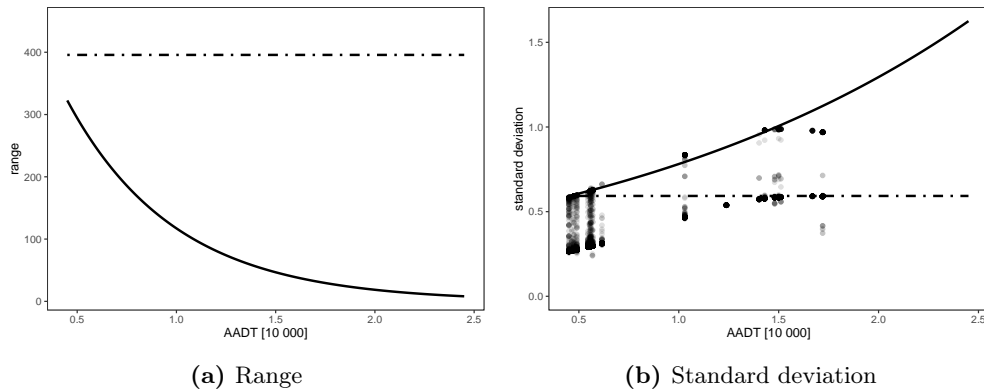
Figure 5.1: Range and standard deviation for the GRF $\xi(s)$ in Model I, with I_S as dotted line, $I_{N\text{-}S}$ solid line and the standard deviation of $\xi_{N\text{-}S}(s)$ at the observation locations as dots. Note that the traffic intensity (AADT) is scaled back to it's actual value.

By assumption, the GRF each year $\xi_j(s)$ is considered a replicate, i.e. realization, of the GRF $\xi(s)$. We fit Model I_S and $I_{N\text{-}S}$ to each single one of the years 2017-2020, one year at a time, with the year specific random intercept term excluded. The measures of the model fit is displayed in Table 5.2, where there seems to be no difference between the stationary and non-stationary model for 2017, for 2019 the non-stationary model is favourable. Finally for 2018 and 2020 the non-stationary is clearly a better fit, with large differences in DIC, CPO and log likelihood, compared with the stationary model. It is no clear tendency for the non-stationary model being superior for all the years, posterior marginals for the SPDE parameters in Appendix B.1 show large differences between the years, with 2018 and 2020 overall showing most similarity in the posterior marginals. In particular, zero is contained in the credible intervals for $\theta_{f,\tau}$ and $\theta_{f,\kappa}$ for 2017, again indicating a non-stationary model is not reasonable for 2017. Having only four replicates of $\xi(s)$ may not be sufficient to get accurate estimates of the SPDE parameters, considering the large differences seen between the different years. Also Ingebrigtsen et al. (2015) show through simulation studies that the coverage of the SPDE parameters increases as more replicates are added, especially for the spatial range parameters $\theta_{1,\kappa}$ and $\theta_{f,\kappa}$, which are more sensitive to a limited number of replicates.

Table 5.2: DIC, CPO and log likelihood for Model I, when fitting to one single year at a time.

		2017	2018	2019	2020
DIC	I_S	5276.4	9364.9	10861.9	8503.5
	$I_{N\text{-}S}$	5270.6	8868.6	10830.2	8320.5
CPO	I_S	2741.3	4691.6	5468.1	4267.2
	$I_{N\text{-}S}$	2740.2	4552.7	5448.0	4232.3
Log likelihood	I_S	-2965.0	-4840.2	-5889.2	-4380.3
	$I_{N\text{-}S}$	-2964.2	-4734.3	-5882.5	-4324.7

Moving to Model II, with an additional GRF $\omega(s)$ representing the pavement stress, we find the estimated parameters and 95% credible interval from the stationary and non-stationary Model II fitted to data 2017-2020 in Table 5.3. There are no differences for β and τ_ϵ, and only slight differences between the stationary and non-stationary model for $\theta_{1,\tau,\xi}$, $\theta_{1,\kappa,\xi}$, $\theta_{1,\tau,\omega}$ and $\theta_{1,\kappa,\omega}$. Recall from Section 4.2 that now the interpretation of $\xi(s)$ is describing the annual spatial deviation from the pavement stress $\omega(s)$. The parameters $\theta_{f,\tau,\xi}$ and $\theta_{f,\kappa,\xi}$ both have credible intervals containing zero, indicating that the annual spatial deviation from $\omega(s)$ might not have a non-stationary nature. Non-stationarity for the pavement stress $\omega(s)$, seems reasonable by the credible intervals of $\theta_{f,\tau,\omega}$ and $\theta_{f,\kappa,\omega}$, although pretty wide, neither contains zero. The possible non-stationary nature of the rutting indicated by Model $I_{N\text{-}S}$ now seems to be captured by the GRF for the pavement stress.

Table 5.3: Posterior mean and 95% credible interval of the hyperparameters and fixed effect, from Model II_S and $II_{N\text{-}S}$ fitted to rutting 2017-2020.

	Model	mean		95% CI	
		II_S	$II_{N\text{-}S}$	II_S	$II_{N\text{-}S}$
β		1.19	1.19	(1.10, 1.27)	(1.09, 1.28)
$\theta_{1,\tau,\xi}$		8.37	8.31	(8.05, 8.69)	(7.96, 8.67)
$\theta_{1,\kappa,\xi}$		-5.74	-5.69	(-5.95, -5.53)	(-5.94, -5.44)
$\theta_{f,\tau,\xi}$			0.14		(-0.69, 1.07)
$\theta_{f,\kappa,\xi}$			-0.14		(-0.80, 0.45)
$\theta_{1,\tau,\omega}$		6.14	6.34	(5.57, 6.70)	(5.80, 6.91)
$\theta_{1,\kappa,\omega}$		-3.56	-3.56	(-3.93, -3.18)	(-3.96, -3.19)
$\theta_{f,\tau,\omega}$			-1.84		(-2.71, -1.06)
$\theta_{f,\kappa,\omega}$			0.75		(0.27, 1.27)
τ_ϵ		1.38	1.39	(1.34, 1.42)	(1.35, 1.43)

The range and marginal variance for the annual spatial deviation from $\omega(s)$ is displayed in Figure 5.2. The range in the stationary case is 1077 m, and 1025 m at the base level in the non-stationary case, and increasing as the

traffic intensity increases, with range equal to the stationary case for a traffic intensity of 8000 AADT. The marginal standard deviation is 0.63 mm in the stationary case and 0.62 mm at the base level in the non-stationary case, with a slight increase for increasing traffic intensity.

The range and marginal variance for $\omega(s)$ is displayed in Figure 5.3. The range is 121 m in both the stationary case and at the base level in the non-stationary case, which decreases with increasing traffic intensity. At the maximum observed traffic intensity the range has dropped to 47 m. In the stationary case the marginal standard deviation is 0.22 mm, and 0.18 mm at the base level in the non-stationary case. The marginal standard deviation for the non-stationary case has increased to 0.56 mm at the maximum observed traffic intensity.
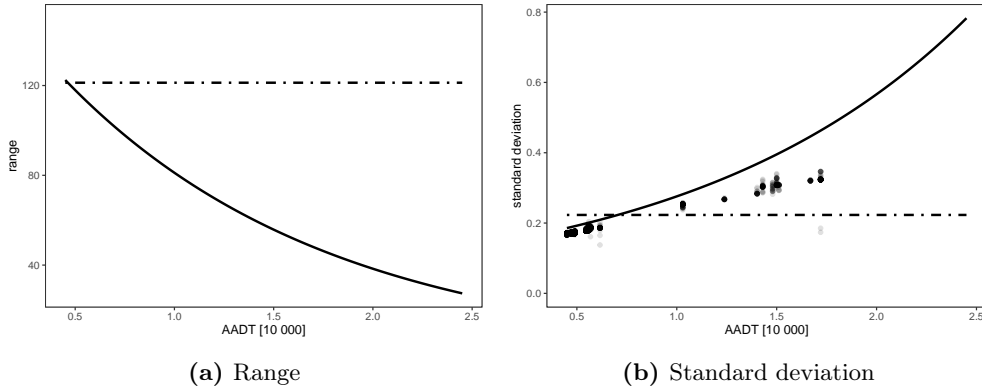

(a) Range

(b) Standard deviation
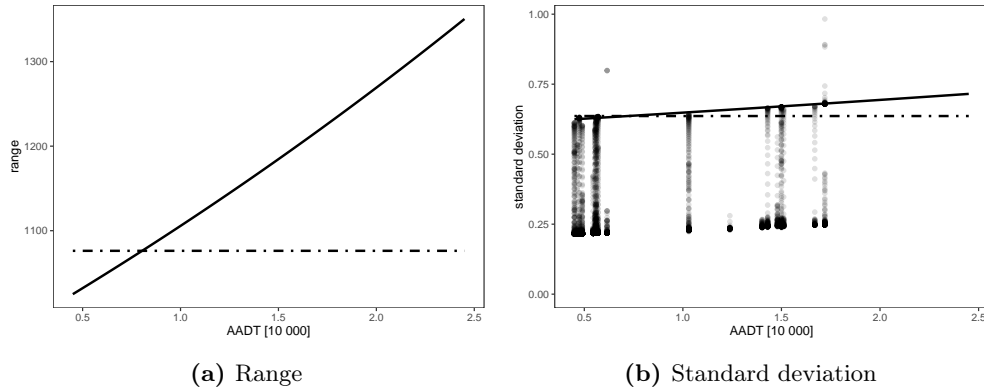
Figure 5.2: Range and standard deviation for the GRF $\xi(s)$ in Model II, with II_S as dotted line, $II_{N\text{-}S}$ solid line and the standard deviation of $\xi_{N\text{-}S}(s)$ at the observation locations as dots. Note that the traffic intensity (AADT) is scaled back to it's actual value.

5.1.2 Model comparison

The most obvious comparison between the proposed models are conducted by considering the model selection criterion's displayed in Table 5.4, we see that for both Model I and II all the measures of fit, DIC, CPO and log likelihood, indicate a better fit for the two non-stationary models, each compared to it's corresponding stationary model. Comparing Model I and II we see that $II_{N\text{-}S}$ are found to be inferior to both I_S and $I_{N\text{-}S}$ by all measures of fit, and the added complexity of $II_{N\text{-}S}$ does not result in an overall increase in model fit.

A further assessment of the model fit is seen in Figure 5.4 where difference in CPO for each road segment is compared between different models, note that we have described the road in one dimension, i.e. stretched it out and let each road segment be 20 m apart in the horizontal direction, in Figure 5.4a the actual road in two-dimensions is displayed with the traffic intensity. The difference in CPO for each road segment and year, i.e. CPO_{ij}, between Model
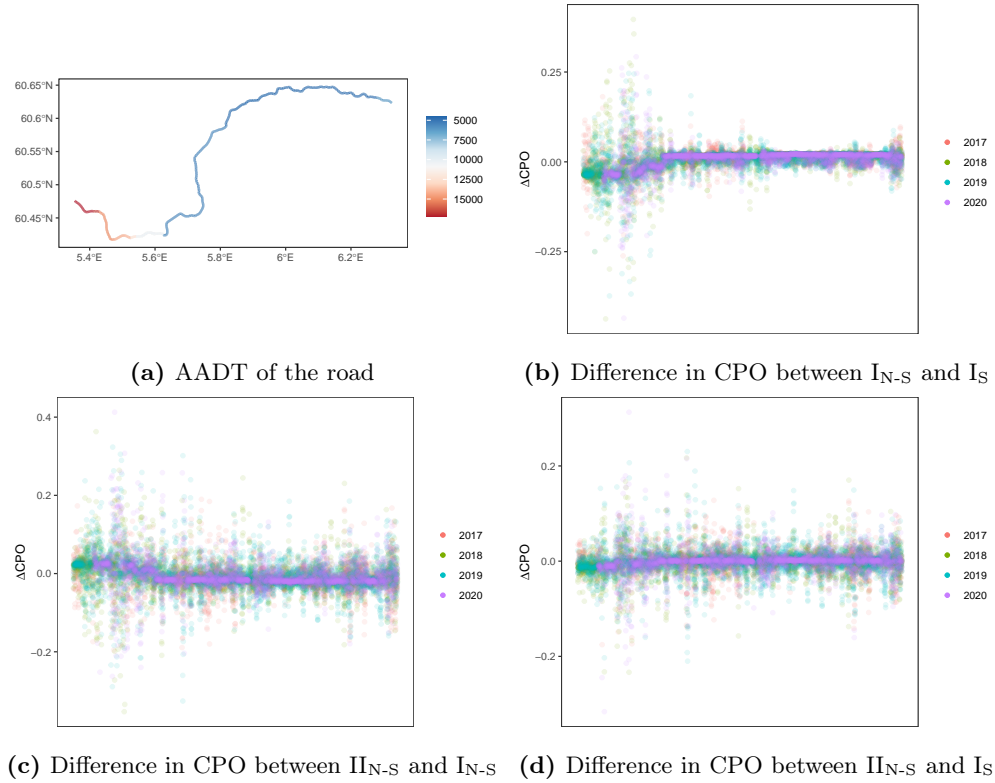
(a) Range

(b) Standard deviation

Figure 5.3: Range and standard deviation for the GRF $\omega(s)$ in Model II, with II_S as dotted line, $II_{N\text{-}S}$ solid line and the standard deviation of $\omega_{N\text{-}S}(s)$ at the observation locations as dots. Note that the traffic intensity (AADT) is scaled back to it's actual value.

$I_{N\text{-}S}$ and I_S is shown in Figure 5.4b, where positive values indicate a better fit of $I_{N\text{-}S}$. The results are somewhat surprising, as the stationary model overall seems to be slightly better at the highest traffic intensities, but with large deviations between which model seems preferable. Whereas the non-stationary provide a slightly better fit at the large proportion of the road with low traffic intensity, although they are very similar at low traffic intensities, consistent with the results in Figure 5.1. The difference between Model $II_{N\text{-}S}$ and $I_{N\text{-}S}$ in Figure 5.4c show that $II_{N\text{-}S}$ is better for high traffic intensities, but still with large deviations, and $I_{N\text{-}S}$ still slightly better at lower traffic intensities, but now with larger deviations. In Figure 5.4d we see that there is no clear visible pattern between the differences of Model $II_{N\text{-}S}$ and I_S, other than several locations with large deviations where the preference of either models change rapidly. There are no visible difference between the years.

Table 5.4: DIC, CPO and log likelihood for Model I_S, $I_{N\text{-}S}$, II_S and $II_{N\text{-}S}$ fitted to rutting 2017-2020.

		Model I	Model II
DIC	S	35597.6	35803.5
	N-S	34958.2	35699.5
CPO	S	17624.3	17742.4
	N-S	17406.1	17699.3
Log likelihood	S	-18399.0	-18436.9
	N-S	-18365.7	-18426.5

Although both I_S and $I_{N\text{-}S}$ seem to fit the data better than II_S and $II_{N\text{-}S}$, the GRF $\omega(s)$, representing the pavement stress, of the latter two has tractable properties in terms of interpreting the deterioration at different locations of

(a) AADT of the road

(b) Difference in CPO between $I_{N\text{-}S}$ and I_S

(c) Difference in CPO between $II_{N\text{-}S}$ and $I_{N\text{-}S}$

(d) Difference in CPO between $II_{N\text{-}S}$ and I_S
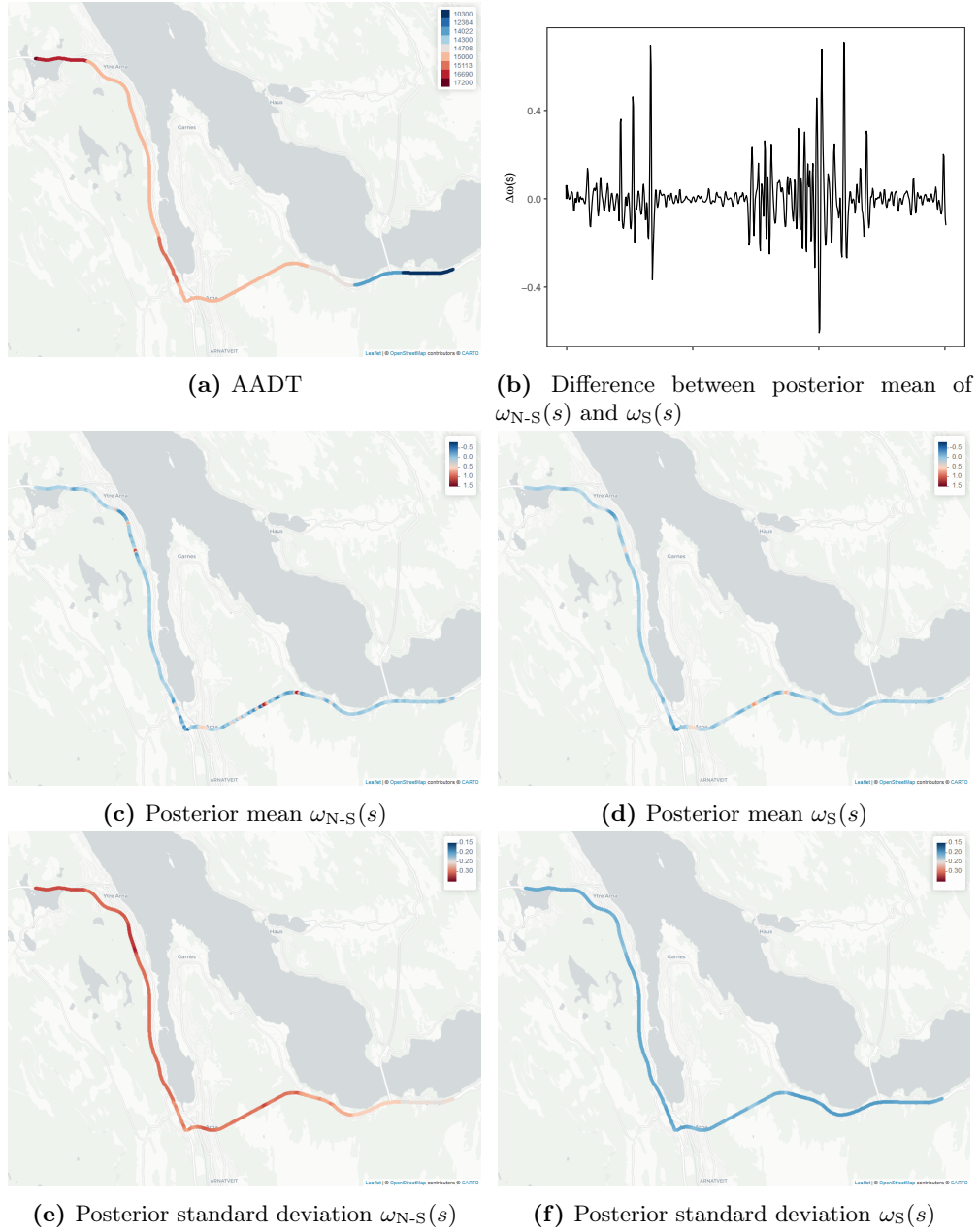
Figure 5.4: Difference in CPO, at each road segment, each year, orientation west to east.

the road during the observation period. In Figure 5.5 the posterior mean and standard deviation of the GRF representing the pavement stress from II_S and $II_{N\text{-}S}$ is displayed for a subset of the road where the traffic intensity has rapid changes. The posterior mean of the GRF from II_S show a higher degree of smoothing, whereas the GRF from $II_{N\text{-}S}$ show greater deviations and more clearly highlighting possible locations with elevated pavement stress. We also observe large differences in the posterior standard deviation, with the overall trend in the non-stationary case of increasing standard deviation as the traffic intensity increases, as expected from Figure 5.3.

The η_i's from Model $I_{N\text{-}S}$ and $II_{N\text{-}S}$ in Figure 5.6 clearly show that the structured additive predictor of $I_{N\text{-}S}$ has more rapid changes specifically in the regions with higher traffic intensity, to the left in the plots, indicating that the traffic intensity influence the dependence structure in a stronger way than compared to Model $II_{N\text{-}S}$. But we also saw from the CPO values in Figure 5.4c that Model $II_{N\text{-}S}$ in general fitted the data better than $I_{N\text{-}S}$ in these high traffic regions of the road, thus the non-stationarity of $I_{N\text{-}S}$ might be overestimated.

Summarising the case study for rutting there are no unique model performing better at all the different parts of the road, overall Model $I_{N\text{-}S}$ shows

(a) AADT

(b) Difference between posterior mean of $\omega_{\text{N-S}}(s)$ and $\omega_{\text{S}}(s)$

(c) Posterior mean $\omega_{\text{N-S}}(s)$

(d) Posterior mean $\omega_{\text{S}}(s)$

(e) Posterior standard deviation $\omega_{\text{N-S}}(s)$

(f) Posterior standard deviation $\omega_{\text{S}}(s)$

Figure 5.5: Properties of the pavement stress $\omega(s)$ in the stationary and non-stationary case, for a subset of the road, of 600 road segments, with values of the pavement stress field projected onto each single road segment.

best fit to the data, but with possible overestimation of the traffic intensity's influence on the dependence structure of $\xi_{\text{N-S}}(s)$. The increased complexity in Model II does not contribute to a better fit considering the whole road, but Model II$_{\text{N-S}}$ show interesting results and model fit equal to or better than I$_{\text{S}}$

(a) 2017

(b) 2018

(c) 2019

(d) 2020
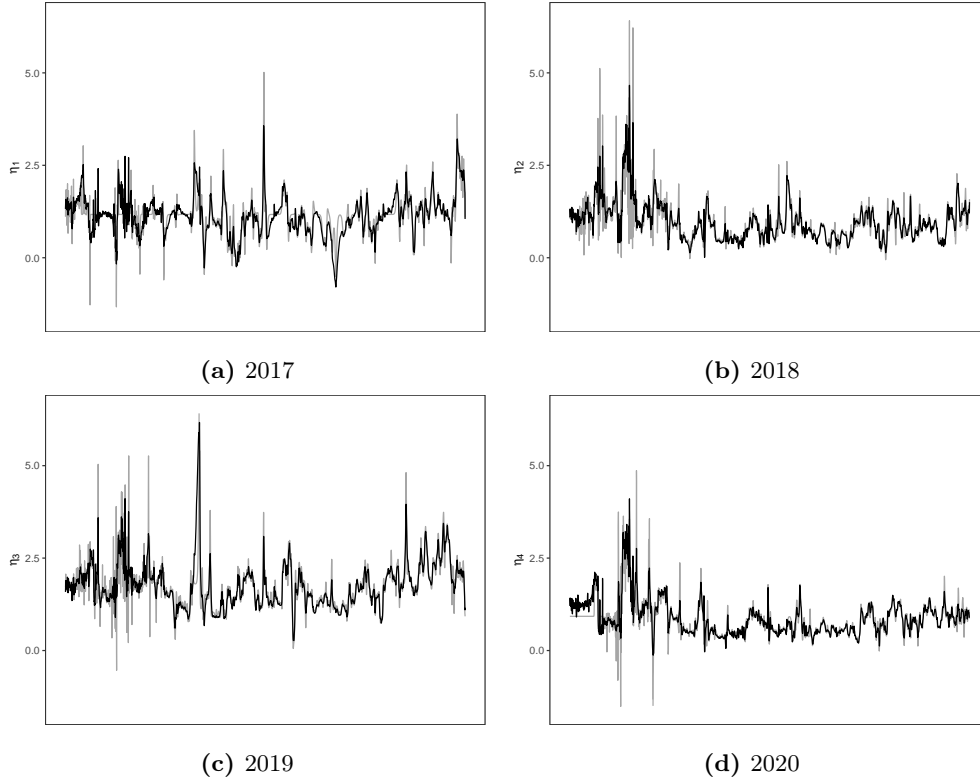
Figure 5.6: η_i in mm for Model $I_{\text{N-S}}$ and $II_{\text{N-S}}$ for each year 2017-2020. $\eta_{i,\text{N-S,I}}$ is represented by grey lines and $\eta_{i,\text{N-S,II}}$ black lines.

and $I_{\text{N-S}}$ for high traffic intensities. In addition the pavement stress $\omega_{\text{N-S}}(s)$ highlights locations with elevated pavement stress in the period under study, and model fit for high traffic intensities indicate that this may be utilized in maintenance planning at particularly these subsets of the road.

5.2 Simulation study

In order to assess the models ability to separate between stationarity and non-stationarity we conduct a simulation study, where the purpose is to investigate model I_S and $I_{\text{N-S}}$'s ability to separate data generated from a stationary and non-stationary GRF, with the procedure given in Section 4.3.

The coverage for all parameters when fitting Model I_S and $I_{\text{N-S}}$ to data simulated from a stationary and non-stationary process are given in Table 5.5. For stationary data we see that the coverage is similar between the two models, and most of the time Model $II_{\text{N-S}}$ correctly imply stationarity, with a coverage of 0.83 for $\theta_{f,\tau}$ and 0.86 for $\theta_{f,\kappa}$. Moving to the non-stationary data, we observe poor coverage for all parameters of Model I_S, with zero for $\theta_{1,\tau}$ and $\theta_{1,\kappa}$, except for β, whereas the coverage for parameters of Model $I_{\text{N-S}}$

Table 5.5: Credible interval coverage for parameters of I_S and $I_{N\text{-}S}$ from fitting the models to rutting simulated from a stationary and non-stationary GRF $\xi(s)$.

Data	stationary		non-stationary	
	I_S	$I_{N\text{-}S}$	I_S	$I_{N\text{-}S}$
β	0.94	0.94	0.87	0.85
$\theta_{1,\tau}$	0.90	0.89	0	0.90
$\theta_{1,\kappa}$	0.91	0.94	0	0.90
$\theta_{f,\tau}$		0.83		0.83
$\theta_{f,\kappa}$		0.86		0.84
τ_ϵ	0.71	0.70	0.31	0.66

is retained, with a decrease for some of the parameters. Overall the coverage is only modest, where estimating the marginal posteriors of the parameters controlling the non-stationarity is a problem in both cases. Model $I_{N\text{-}S}$ seems, in most cases, to be able to separate data generated from a stationary and non-stationary GRF reasonably well.

Looking at the measures of fit in Figure 5.7a, displaying the difference in DIC and CPO between Model $I_{N\text{-}S}$ and I_S for the stationary data, we see very similar measures of fit for the two models. For the non-stationary data in Figure 5.7b, the median of the difference in CPO is -290 and DIC -605, indicating a clear preference for Model $I_{N\text{-}S}$ over I_S.

(a) Stationary data (b) Non-stationary data
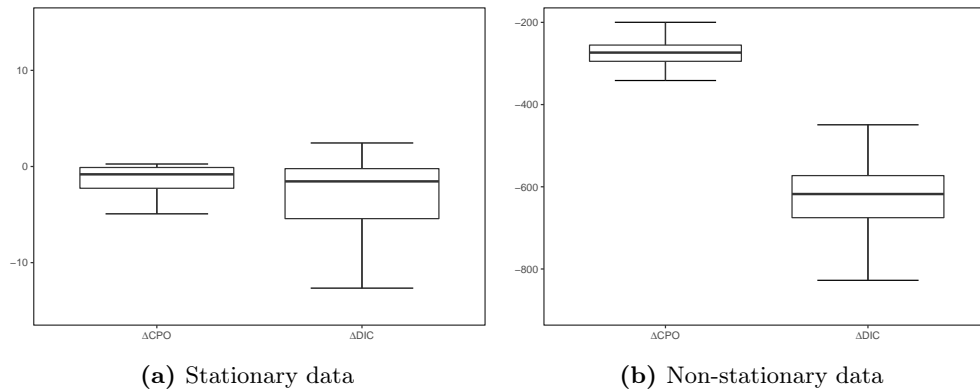
Figure 5.7: Difference in CPO and DIC between $I_{N\text{-}S}$ and I_S fitted to rutting simulated from a stationary and non-stationary GRF $\xi(s)$.

The marginal posterior means are shown in Figure 5.8, with the true values given by red dots. Although we saw less than ideal coverage for most of the parameters, the overall spread does not seem to be very high, and for the SPDE parameters the implications for the nature of the GRF may not necessarily be very large. We notice in particular from Figure 5.8b that the parameters $\theta_{1,\tau}$ and $\theta_{1,\kappa}$, miss the actual parameter value, as the coverage are 0 for both, but

they are not very far of, indicating that the range and standard deviation of the GRF will be fairly similar at the base level traffic intensity. In addition we observe that the posterior marginal means of $\theta_{f,\tau}$ varies more around the true parameter value than $\theta_{f,\kappa}$, for both stationary and non-stationary data.
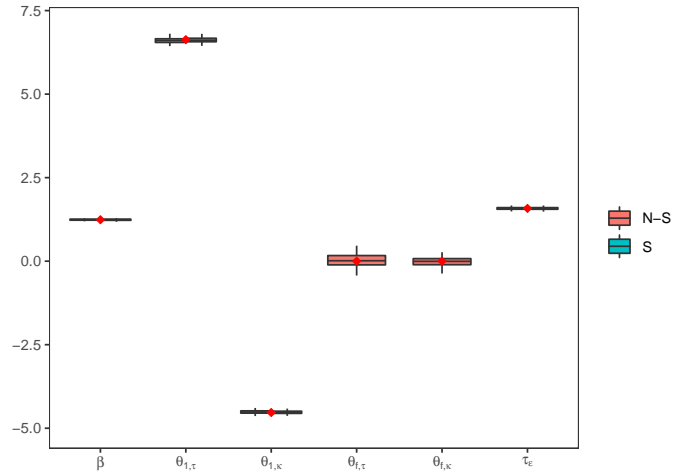
(a) Stationary data
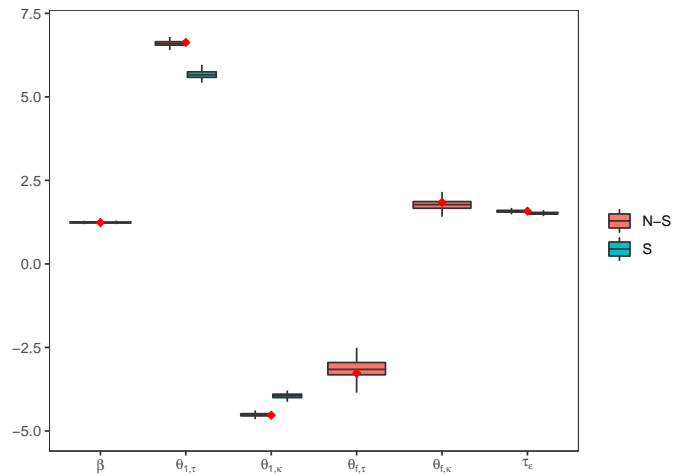
(b) Non-stationary data

Figure 5.8: Boxplot of marginal posterior means for parameters of I_S and $I_{N\text{-}S}$ fitted to rutting simulated from a stationary and non-stationary GRF $\xi(s)$. With the true parameter values of the simulated data given by red dots.

5.3 Prior sensitivity

We now make a brief investigation of how the approach for setting informative priors for the SPDE parameters fares compared to a more naive non-informative approach. The prior sensitivity for varying the values of c_ρ and c_σ were shown by Ingebrigtsen et al. (2015) to be stable, when five replicates of the GRF were used, compared to only one replicate, with more unstable results. Instead we consider the case were we don't have any prior information about the spatial process, and default to non-informative priors for the SPDE parameters. We look at the two non-stationary models, Model $I_{\text{N-S}}$ and $II_{\text{N-S}}$, along with three different designs, A, B and C with different priors for the SPDE parameters, all of which are given in Appendix B.2. The priors for the other parameters β, τ_γ and τ_ϵ are set according to the priors in Section 4.2.2, for all three prior designs.

5.3.1 Model I

Design A is a fully non-informative approach where we let the priors be given as

$$\theta_{1,\tau,\xi}, \theta_{1,\kappa,\xi} \overset{iid}{\sim} \mathcal{N}(0, 10),$$
$$\theta_{f,\tau,\xi}, \theta_{f,\kappa,\xi} \overset{iid}{\sim} \mathcal{N}(0, 2),$$

where the variance for the priors of the SPDE parameters cannot be chosen to high, in order to avoid numerical issues, as mentioned in Section 4.2.2.

In design B we take a semi-informative approach for setting the priors, by using the marginal posterior means from design A as prior means. We keep the results of the simulation study in Section 5.2 in mind, as we observed a coverage of 0 for $\theta_{1,\tau}$ and $\theta_{1,\kappa}$ when the data were generated from a non-stationary process. Thus we need to ensure that the prior variance is sufficiently high in this design, and refrain from using the marginal posterior variances from the results of design A, keeping the variance of the priors the same, i.e. 10 and 2.

Design C is simply Model $I_{\text{N-S}}$ with priors as specified in Section 4.1.2, and results presented in Section 5.1.

Marginal posterior means and 95% credible intervals for the parameters from the three prior designs are presented in Table 5.6, we see that the results from design A in particular deviate from design C in terms of the SPDE parameters controlling the non-stationarity, $\theta_{f,\tau}$ and $\theta_{f,\kappa}$. This difference is decreased when we move on to design B, and it seems that supplying some information about the parameters $\theta_{1,\tau}$ and $\theta_{1,\kappa}$ lead to big changes in the marginal posteriors for $\theta_{f,\tau}$ and $\theta_{f,\kappa}$, now indicating non-stationarity in a manner similar to that of design C, but still with considerable differences. We need to stress that the posterior marginals in design C by no means are the correct ones, and the comparison with respect to design C is merely an examination

of the prior sensitivity when fitting model I_{N-S}, with different priors, to the actual rutting data.

Table 5.6: Marginal posterior means and 95% credible intervals for parameters of Model I_{N-S} with three different prior designs for the SPDE parameters.

		mean			95% CI		
	Design	A	B	C	A	B	C
β		1.21	1.20	1.24	(0.18, 1.47)	(1.58, 1.69)	(0.92, 1.56)
$\theta_{1,\tau}$		7.00	6.20	6.63	(6.02, 6.40)	(6.87, 7.17)	(6.13, 7.00)
$\theta_{1,\kappa}$		-4.69	-4.26	-4.53	(-4.83, -4.60)	(-4.38, -4.15)	(-4.76, -4.23)
$\theta_{f,\tau}$		-0.23	-2.62	-3.27	(-1.36, 0.50)	(-2.93, -2.30)	(-3.62, -2.92)
$\theta_{f,\kappa}$		-0.10	1.44	1.84	(-0.64, 0.73)	(1.25, 1.61)	(1.64, 2.04)
τ_{γ}		7.34	10.47	10.80	(1.31, 19.95)	(2.21, 28.20)	(2.26, 29.05)
τ_{ϵ}		1.42	1.64	1.58	(1.38, 1.47)	(1.58, 1.69)	(1.53, 1.64)

5.3.2 Model II

We use the same prior designs for examining the prior sensitivity of Model II_{N-S} as introduced for Model I_{N-S}, with only minor adjustments. In design A we set the priors

$$\theta_{1,\tau,\xi}, \theta_{1,\kappa,\xi}, \theta_{1,\tau,\omega}, \theta_{1,\kappa,\omega} \overset{iid}{\sim} \mathcal{N}(0, 2.5),$$

$$\theta_{f,\tau,\xi}, \theta_{f,\kappa,\xi}, \theta_{f,\tau,\omega}, \theta_{f,\kappa,\omega} \overset{iid}{\sim} \mathcal{N}(0, 2),$$

notice the decreased variance compared to design A for Model I_{N-S}, again, this is due to the numerical issues regarding the optimisation routine in `R-INLA`. The inclusion of $\omega_{N-S}(s)$ increases the hyperparameter space, and we encounter numerical issues very quickly if the variance of the priors exceed the values set here. Design B use the marginal posterior means from the results of design A above, keeping the variance of the priors as in design A. Design C is Model II_{N-S} with priors as specified in Section 4.1.2, and results presented in Section 5.1.

The results from using three different prior designs for Model II_{N-S} are given in 5.7, starting with design A and the parameters of $\xi_{N-S}(s)$ we see that the posterior marginals clearly have moved away from the priors, for all four, and the parameters of $\omega_{N-S}(s)$ show the same tendency as seen for design A in Model I_{N-S}, in regards to the parameters controlling the non-stationarity, $\theta_{f,\tau,\omega}$ and $\theta_{f,\kappa,\omega}$ not indicating any non-stationarity. Moving on to design B we see the same tendency as earlier, were the posterior marginals of the parameters controlling the non-stationarity of the GRF's are influenced to a greater extent than with the priors given by design A. Note that the differences compared to design C is now considerable, indicating a whole different kind of non-stationarity, that is, the annual spatial deviation $\xi(s)$ from the pavement stress

Table 5.7: Marginal posterior means and 95% credible intervals for parameters of Model II$_{\text{N-S}}$ with three different prior designs for the SPDE parameters.

		mean			95% CI		
Design		A	B	C	A	B	C
β		1.11	1.13	1.19	(1.00, 1.23)	(0.99, 1.26)	(1.09, 1.28)
$\theta_{1,\tau,\xi}$		7.10	7.44	8.31	(6.89, 7.32)	(6.93, 7.81)	(7.96, 8.67)
$\theta_{1,\kappa,\xi}$		-4.87	-5.10	-5.69	(-5.02, -4.73)	(-5.33, -4.79)	(-5.94, -5.44)
$\theta_{f,\tau,\xi}$		-4.69	-5.51	0.14	(-4.98, -4.40)	(-5.84, -5.18)	(-0.69, 1.07)
$\theta_{f,\kappa,\xi}$		2.78	3.27	-0.14	(2.64, 2.93)	(3.10, 3.44)	(-0.80, 0.45)
$\theta_{1,\tau,\omega}$		10.00	11.01	6.34	(9.14, 10.77)	(10.11, 12.19)	(5.80, 6.91)
$\theta_{1,\kappa,\omega}$		-6.23	-6.93	-3.56	(-6.81, -5.58)	(-7.81, -6.25)	(-3.96, -3.19)
$\theta_{f,\tau,\omega}$		-0.50	-1.65	-1.84	(-1.54, 0.68)	(-3.21, -0.46)	(-2.71, -1.06)
$\theta_{f,\kappa,\omega}$		-0.25	0.54	0.75	(-1.24, 0.61)	(-0.47, 1.85)	(0.27, 1.27)
τ_ϵ		1.57	1.54	1.39	(1.52, 1.62)	(1.49, 1.54)	(1.35, 1.43)

$\omega(s)$ seems to be non-stationary, and possible non-stationarity of the pavement stress is more ambiguous. The implications for the nature of the field $\omega_{\text{N-S}}(s)$ is a higher degree of smoothing, while $\xi_{\text{N-S}}(s)$ shows larger and more rapid fluctuations, especially for high traffic intensities. The smoothing of $\omega_{\text{N-S}}(s)$ is clear from Figure 5.9, where the pavement stress for Design A and B are considerably smoother compared to Design C. This difference is attributed to the spatial range of the pavement stress, at the base level traffic intensity it is 1759 m and 3542 m for Design A and B, whereas for Design C only 121 m.

In addition the hyperparameter space of Model II$_{\text{N-S}}$ is nine dimensional, further complicating the optimisation routine in `R-INLA`, posing restrictions on how vague the hyperpriors can be without getting into numerical issues. We also observe that the approach for setting informative priors, in design C, might impose to restrictive priors, where $\theta_{1,\tau,\xi}$ and $\theta_{1,\tau,\omega}$ have a prior variance of 1.06, and $\theta_{1,\kappa,\xi}$ and $\theta_{1,\kappa,\omega}$ a prior variance of 0.51.
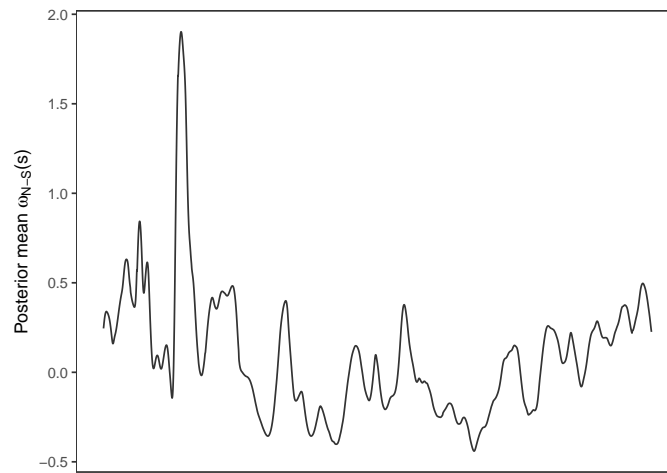
(a) Design A
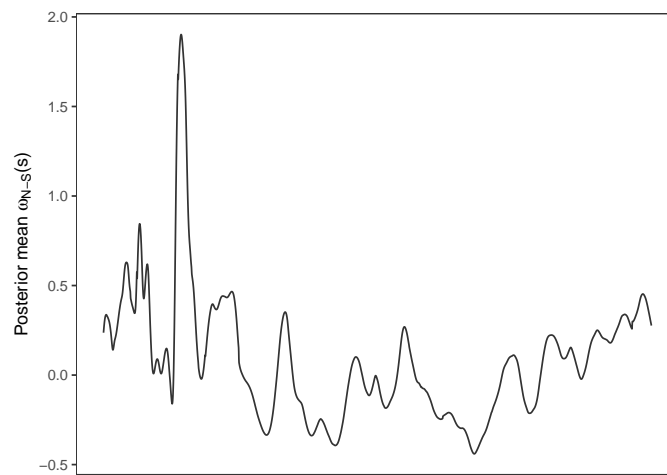
(b) Design B
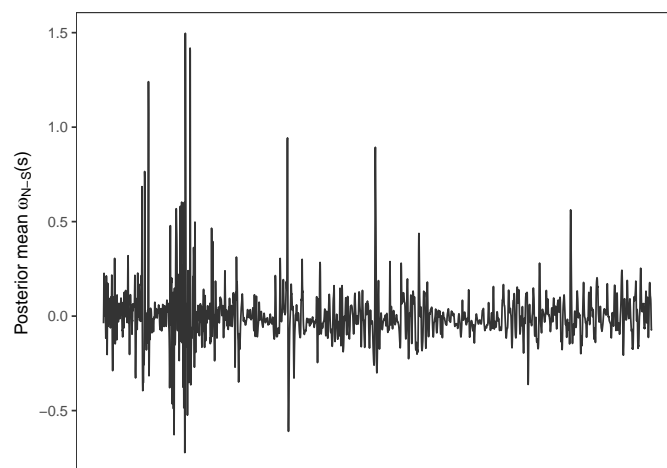
(c) Design C

Figure 5.9: Posterior mean of the non-stationary pavement stress $\omega_{\text{N-S}}(s)$ from Model $\text{II}_{\text{N-S}}$ fitted to rutting 2017-2020 with prior Design A, B and C.

Chapter 6

Results: Traffic accidents

In this chapter we present the results from fitting the models introduced in Section 4.2 for the occurrence of accidents. The models are compared in terms of the marginal posteriors of the parameters and their implication of a potential underlying process, in addition to the models fit to the data.

The models' ability to separate data generated from a spatial stationary and non-stationary process is investigated in a simulation study, as described in Section 4.3.

6.1 Case study

The stationary and non-stationary model introduced in Section 4.2 are fitted to the observations of an accident occurring within a road segment in the period 2015-2020, with prior distributions of the parameters given in 4.2.2.

The marginal posterior means and 95% credible interval of the intercept and SPDE parameters are shown in Table 6.1. We observe exactly the same results between the two models for the intercept β, for the SPDE parameters $\theta_{1,\tau}$ and $\theta_{1,\kappa}$ there are considerable differences between the models, with wide credible intervals, all except for $\theta_{1,\kappa,S}$ containing zero, and no clear indication of the nature of the GRF. The same results goes for the parameters $\theta_{f,\tau}$ and $\theta_{f,\kappa}$, neither indicating any non-stationarity. The estimated parameters indicate an extremely low spatial range, below 1 m, considered highly unlikely, indicating no spatial correlation between neighbouring segments.

The measures of fit in Table 6.1 show no discernable difference between the stationary and non-stationary model. A closer investigation show low CPO values at all road segments with accidents, and very high values at all other road segments, for both models, implying that neither of the models seem to pick up any information regarding the accident locations. We note that the number of accidents, 44, relative to the number of road segments, 4030, possibly impart estimation of the marginal posteriors.

There are no signs of any non-stationarity and in excess of any other explanatory variables the GRF does not seem to capture any unobserved information

Table 6.1: Posterior mean and 95% credible interval of the hyperparameters and fixed effect, from Model I_S and I_{N-S} fitted to accidents 2015-2020.

		mean		95% CI	
Model	I_S	I_{N-S}		I_{N-S}	I_{N-S}
β	-4.50	-4.50	(-4.81, -4.22)	(-4.81, -4.22)
$\theta_{1,\tau}$	0.36	1.79	(-4.53, 3.44)	(-0.45, 4.54)
$\theta_{1,\kappa}$	4.97	1.82	(2.54, 9.53)	(-0.36, 4.54)
$\theta_{c,\tau}$		0.81		(-1.59, 3.22)
$\theta_{c,\kappa}$		0.89		(-1.51, 3.30)

Table 6.2: DIC, CPO and log likelihood from Model I_S and I_{N-S} fitted to accidents 2015-2020.

	I_S	I_{N-S}
DIC	487.03	487.03
CPO	243.52	243.52
Log likelihood	-247.87	-247.90

regarding the event of accident or not either.

6.2 Simulation study

In line with the simulation study in Section 5.2, we investigate if the models are able to distinguish between data generated from a stationary and non-stationary process, with the procedure described in Section 4.3.

We experience the same results as in the case study, in regards to separating the two models. Results from the simulation study are shown in Appendix C, where none of the models are able to cover the true parameter values or identifying whether the data are generated from a stationary or non-stationary process. The differences in measures of fit shows no clear preference for either models. These results are the same for both the two simulated data sets, stationary and non-stationary.

The simulation study is only very brief, but show that the estimation of the SPDE parameters is increasingly difficult when moving to a Bernoulli likelihood, opposed to a Gaussian likelihood in Section 5.2, and extreme care must be taken when fixing the parameters. The influence the SPDE parameters have on the probability of an accident are more complicated with such a likelihood as well, they are connected through the logit link function, and minor changes in the SPDE parameters may lead to a large change in the probability of accident. In particular, letting the marginal and nominal standard deviation of the GRF vary to much with respect to the curvature quickly lead to numerical issues, in the same manner as described in Section 4.2.2 and 5.3.

Chapter 7

Discussion and concluding remarks

In this thesis we investigated the annual change in rut depth, rutting, in addition to the occurrences of accidents, for road segments of 20 meter, along the 80 km road E16 from Bergen to Voss. The spatial dependencies between road segments were investigated, modelled as stationary and non-stationary Gaussian random fields within the latent Gaussian model framework. Where the purpose was two-fold, first, to learn about how the traffic intensity possibly influence the spatial dependence structure of the rutting, and the horizontal curvature for the occurrences of accidents, with the main focus directed to rutting. The second purpose was to develop models capable of highlighting road segments with elevated rutting which may require a physical inspection and possible maintenance.

The main results from evaluating the four proposed models for rutting indicate non-stationarity for the rutting, where the spatial dependence structure varies with the traffic intensity. This is indicated by posterior marginals controlling the non-stationarity being significantly different from zero, in addition to the model selection criterion's DIC, CPO and log likelihood all favouring the two non-stationary models over the corresponding stationary model. No unique model were found to be superior for all different subsets of the road, in particular when considering the high traffic intensity areas against low traffic intensity, the preferred model changes. Within the proposed models and the chosen priors, the effect of increased traffic intensity on the spatial dependence structure show a decrease in spatial range and increase in standard deviation, indicating higher spatial variability in the rutting at high traffic intensities, with the possible consequence being a higher frequency of repaving or other maintenance activities, as indicated by Aurstad et al. (2016) and Bakløkk (2017). For the models with one GRF and four replicates of the spatial field, the simulation study show that the non-stationary model in most cases indicate stationarity when there is no non-stationarity present, with fairly similar indications towards non-stationarity when it is present. Although the results

indicate non-stationarity depending on the traffic intensity for rutting, the type of non-stationarity present is ambiguous, especially for models with two GRFs, and the nature of the GRFs are very prior sensitive, as shown by the prior sensitivity analysis in Section 5.3, with somewhat informative and non-informative priors. As noted by Fuglstad et al. (2015) there is a need to not only determine if there is non-stationarity, but also consider what type of non-stationarity is present, and possibly target this directly and not through flexible models. The prior sensitivity analysis also highlight that some of the priors said to be informative might be too restrictive, and we may also question how informative the chosen priors actually are in the case where we have two GRFs in Model II. The assumption taken in this thesis of setting the same priors for the parameters of these two GRFs is rather weak, and warrants a further investigation.

The aim of highlighting road segments with elevated rutting motivated the inclusion of a GRF for the pavement stress, this field shows tractable properties in terms of locating problematic road segments over time, and the model with non-stationary pavement stress seems to be the one providing the best fit in areas of high traffic intensity. Hence, this may be utilized in maintenance planning for locating possible locations where maintenance is due or a closer physical inspection should be conducted, especially for areas with high traffic intensity. This shows that the inclusion of such a field is useful in terms of interpreting the evolution of the rutting, previously proposed by Ingebrigtsen et al. (2015) for improving forecasting and interpolation with respect to a precipitation process, and used by Ødegård (2017). Aside from the tractable properties of representing the pavement stress by a second GRF, having two GRFs greatly increase the dimension of the hyperparameter space, and numerical issues regarding the numerical optimisation routine in `R-INLA` are likely to appear, where the solution is to decrease the variance of the hyperpriors, thus including a second GRF does not come without additional constraints and more care need to be taken compared to models with one single GRF.

The brief results from considering traffic accidents and including non-stationarity dependent on the curvature are inconclusive, with no signs of non-stationarity, and the stationary and non-stationary model show similar traits with extremely low spatial ranges, lower than the actual length of each road segment. The spatial fields does not seem to pick up any latent unobserved effects, nor any sense of borrowed information between different road segments. The accidents were not the main focus of this study, it was merely an investigation whether the models proposed for rutting could be used within other parts of the road safety domain, motivated by the findings in the preliminary work (Vedvik, 2020) and the lack of prior studies of traffic accident modelling for small spatial units. Thus a more thorough study should be conducted to clarify if the approach possibly can provide any insight, where the first step should be to check in a more thorough manner if data simulated from a non-stationary process actually can be detected as non-stationary by the models. Ziakopoulos and Yannis (2020) points to missing data or difficulties with data

acquisition as a possible cause for the lack of studies at small spatial units, but the sparsity of actual accidents may also cause inferential problems.

The proposed models for rutting do only contain various intercept terms and various GRFs, as the main interest was to investigate possible spatial dependencies and highlight locations with elevated rutting over time, but if the purpose is directed at forecasting the rutting next year, one would possibly include other explanatory variables such as temperature, precipitation, speed limit, pavement age and the use of studded tyres (Saba et al., 2006). Including random intercepts, for each specific road segment or different traffic intensity groups, is another possibility, and if even more years of measurements are available, temporal random effects may be considered for increased forecasting accuracy, treating the evolution of the rutting at different road segment as separate replicates of the temporal effect. The effects should possibly be included in either the stationary or non-stationary Model I, as the hyperparameter space and model complexity of the models containing two GRFs, Model II, is already high and their overall fit to the data worse. Further studies should also consider roads where the distribution of the traffic intensity is more evenly distributed, here around 75% of the road were low traffic intensity areas, and few road segments within each of the high traffic intensities. The measurement errors originating from aggregating annual measurements according to the 2020 measurement locations may be dealt with by considering the actual locations of each single measurement, this would work in the models used in this thesis, but not for some of the alterations proposed here which depend on annual measurements at each road segment.

Bibliography

Aurstad, J., Uthus, N., Telle, R. & Baklokk, L. (2016). The influence of asphalt workmanship on pavement service life.

Bakløkk, L.-J. (2017). *Varige veger: Sluttrapport : Etatsprogrammet varige veger 2011-2015* (tech. rep.). Statens vegvesen.

Banerjee, B. P., Bradley, P. C. & Gelfand, A. E. (2004). *Hierarchical modeling and analysis for spatial data.* Boca Raton, FL: Chapman; Hall/CRC.

Blangiardo, M. & Cameletti, M. (2015). *Spatial and Spatio-temporal Bayesian models with R-INLA*. John Wiley & Sons.

Fuglstad, G.-A., Simpson, D., Lindgren, F. & Rue, H. (2015). Does non-stationary spatial data always require non-stationary random fields? *Spatial Statistics*, *14*, 505–531. https://doi.org/https://doi.org/10.1016/j.spasta.2015.10.001

Galgamuwa, U., Du, J. & Dissanayake, S. (2021). Bayesian spatial modeling to incorporate unmeasured information at road segment levels with the inla approach: A methodological advancement of estimating crash modification factors. *Journal of Traffic and Transportation Engineering (English Edition)*, *8*(1), 95–106. https://doi.org/https://doi.org/10.1016/j.jtte.2019.03.003

Gelfand, A., Diggle, P., Fuentes, M. & Guttorp, P. (2010). Handbook of spatial statistics. *Handbook of Spatial Statistics*. https://doi.org/10.1201/9781420072884

Held, L., Schrödle, B. & Rue, H. (2010). Posterior and cross-validatory predictive checks: A comparison of mcmc and inla. https://doi.org/10.1007/978-3-7908-2413-1_6

Hubin, A. & Storvik, G. (2016). Estimating the marginal likelihood with integrated nested laplace approximation (inla).

Ingebrigtsen, R., Lindgren, F. & Steinsland, I. (2014). Spatial models with explanatory variables in the dependence structure [Spatial Statistics Miami]. *Spatial Statistics*, *8*, 20–38. https://doi.org/https://doi.org/10.1016/j.spasta.2013.06.002

Ingebrigtsen, R., Lindgren, F., Steinsland, I. & Martino, S. (2015). Estimation of a non-stationary model for annual precipitation in southern norway using replicates of the spatial field. *Spatial Statistics*, *14*, 338–364. https://doi.org/https://doi.org/10.1016/j.spasta.2015.07.003

Lea, J. D. & Harvey, J. T. (2015a). A spatial analysis of pavement variability. *International Journal of Pavement Engineering*, *16*(3), 256–267. https://doi.org/10.1080/10298436.2014.942857

Lea, J. D. & Harvey, J. T. (2015b). Using spatial statistics to characterise pavement properties. *International Journal of Pavement Engineering*, *16*(3), 239–255. https://doi.org/10.1080/10298436.2014.942856

Lindgren, F. & Rue, H. (2015). Bayesian spatial modelling with r-inla. *Journal of Statistical Software*, *63*, 1–25. https://doi.org/10.18637/jss.v063.i19

Lindgren, F., Rue, H. & Lindström, J. (2011). An explicit link between Gaussian fields and Gaussian Markov random fields: The stochastic partial differential equation approach. *Journal of the Royal Statistical Society, Series B*, *73*(4), 423–498.

Martins, T. G., Simpson, D., Lindgren, F. & Rue, H. (2013). Bayesian computing with inla: New features. *Computational Statistics & Data Analysis*, *67*, 68–83. https://doi.org/https://doi.org/10.1016/j.csda.2013.04.014

Norwegian government. (2016). *National transport plan 2018–2029*. Retrieved February 5, 2021, from https://www.regjeringen.no/en/dokumenter/meld.-st.-33-20162017/id2546287/

Ødegård, J. (2017). *Spatial non-stationary models for precipitation with elevation in the dependency structure - a case study of annual precipitation in hordaland* (Master's thesis). Norwegian University of Science and Technology.

Pebesma, E. (2018). Simple Features for R: Standardized Support for Spatial Vector Data. *The R Journal*, *10*(1), 439–446. https://doi.org/10.32614/RJ-2018-009

Pettit, L. I. (1990). The conditional predictive ordinate for the normal distribution. *Journal of the Royal Statistical Society: Series B (Methodological)*, *52*(1), 175–184. https://doi.org/https://doi.org/10.1111/j.2517-6161.1990.tb01780.x

R Development Core Team. (2008). *R: A language and environment for statistical computing.* [R Foundation for Statistical Computing. Vienna, Austria].

Rue, H. & Held, L. (2005). Gaussian markov random fields: Theory and applications. *Gaussian Markov Random Fields*, *104*. https://doi.org/10.1201/9780203492024

Rue, H. & Martino, S. (2007). Approximate bayesian inference for hierarchical gaussian markov random field models. *Journal of Statistical Planning and Inference*, *137*(1), 3177–3192.

Rue, H., Martino, S. & Chopin, N. (2009). Approximate bayesian inference for latent gaussian models using integrated nested laplace approximations. *Journal of the Royal Statistical Society, Series B*, *71*(2), 319–392.

Rue, H., Riebler, A., Sørbye, S. H., Illian, J. B., Simpson, D. P. & Lindgren, F. K. (2017). Bayesian computing with inla: A review. *Annual Review*

of Statistics and Its Application, *4*(1), 395–421. https://doi.org/10. 1146/annurev-statistics-060116-054045

Saba, R. G., Huvstig, A., Hildebrand, G., Sund, E., Evensen, R., Sigursteinsson, H. & Elsander, J. (2006). *Performance prediction models for flexible pavements: A state-of-the-art report* (tech. rep.). Statens vegvesen.

Spiegelhalter, D. J., Best, N. G., Carlin, B. P. & Van der Linde, A. (2002). Bayesian measures of model complexityand fit (with discussion). *Journal of the Royal Statistical Society, Series B*, *64*(4), 583–639.

Statens Vegvesen. (2020). *Vegkart*. Retrieved January 20, 2021, from https: //vegkart.atlas.vegvesen.no/

Statistics Norway. (2020). *Road traffic accidents involving personal injury*. Retrieved February 6, 2021, from https://www.ssb.no/en/transport-og-reiseliv/statistikker/vtu/aar

Stein, M. L. (1999). *Interpolation of spatial data* (1st ed.). Springer-Verlag New York.

Sund, E. K. (2012). *Hva vil det koste å fjerne forfallet på riksvegnettet? : Resultat av kartlegging* (tech. rep.). Statens vegvesen.

Sund, E. K. (2013). *Hva vil det koste å fjerne forfallet på fylkesvegnettet? : Resultat av kartlegging* (tech. rep.). Statens vegvesen.

Svenson, K., li, Y., Macuchova, Z. & Rönnegård, L. (2016). Evaluating needs of road maintenance in sweden with the mixed proportional hazards model. *Transportation Research Record: Journal of the Transportation Research Board*, *2589*, 51–58. https://doi.org/10.3141/2589-06

Vedvik, E. (2020). Modelling road traffic accidents with spatial dependencies.

Wickham, H. (2016). *Ggplot2: Elegant graphics for data analysis*. Springer-Verlag New York. https://ggplot2.tidyverse.org

Zhao, B., Silva, E. & Soga, K. (2019). Pavement degradation: A city-scale model for san francisco. *Proceedings of the Institution of Civil Engineers - Smart Infrastructure and Construction*, *171*, 1–57. https://doi.org/ 10.1680/jsmic.18.00001

Ziakopoulos, A. & Yannis, G. (2020). A review of spatial approaches in road safety. *Accident Analysis and Prevention*, *135*(1).

Appendix A

Laplace approximation

The Laplace approximation is an approximation to an integral by use of the Laplace method, following Blangiardo and Cameletti (2015), suppose we are interested in computing the integral

$$\int f(x)\,\mathrm{d}x = \int \exp\bigl(\log f(x)\bigr)\,\mathrm{d}x,$$

where $f(x)$ denotes the density function of a random variable X.

Let $\log f(x)$ be represented by a second order Taylor series expansion around $x = x_0$. Setting x_0 equal to the mode $x^* = \operatorname{argmax}_x \log f(x)$, the second term $\partial \log f(x)/\partial x \big|_{x=x^*}$, of the Taylor series expansion vanishes and the approximation becomes

$$\log f(x) \approx \log f(x^*) + \frac{(x-x^*)^2}{2} \frac{\partial^2 \log f(x)}{\partial^2 x}\bigg|_{x=x^*}.$$

The integral can now be approximated as

$$\int f(x)\,\mathrm{d}x \approx \exp\bigl(\log f(x^*)\bigr) \int \exp\left(\frac{(x-x^*)^2}{2} \frac{\partial^2 \log f(x)}{\partial^2 x}\bigg|_{x=x^*}\right)\mathrm{d}x,$$

letting $\sigma^{2*} = -1/\frac{\partial^2 \log f(x)}{\partial^2 x}\big|_{x=x^*}$ we obtain

$$\int f(x)\,\mathrm{d}x \approx \exp\bigl(\log f(x^*)\bigr) \int \exp\left(-\frac{(x-x^*)^2}{2\sigma^{2*}}\bigg|_{x=x^*}\right)\mathrm{d}x,$$

and recognize the integrand as the kernel of a Normal distribution with mean x^* and variance σ^{2*}. The integral evaluated in the interval (a,b) is approximated by

$$\int_a^b f(x)\,\mathrm{d}x \approx f(x^*)\sqrt{2\pi\sigma^{2*}}\bigl(\Phi(b) - \Phi(a)\bigr),$$

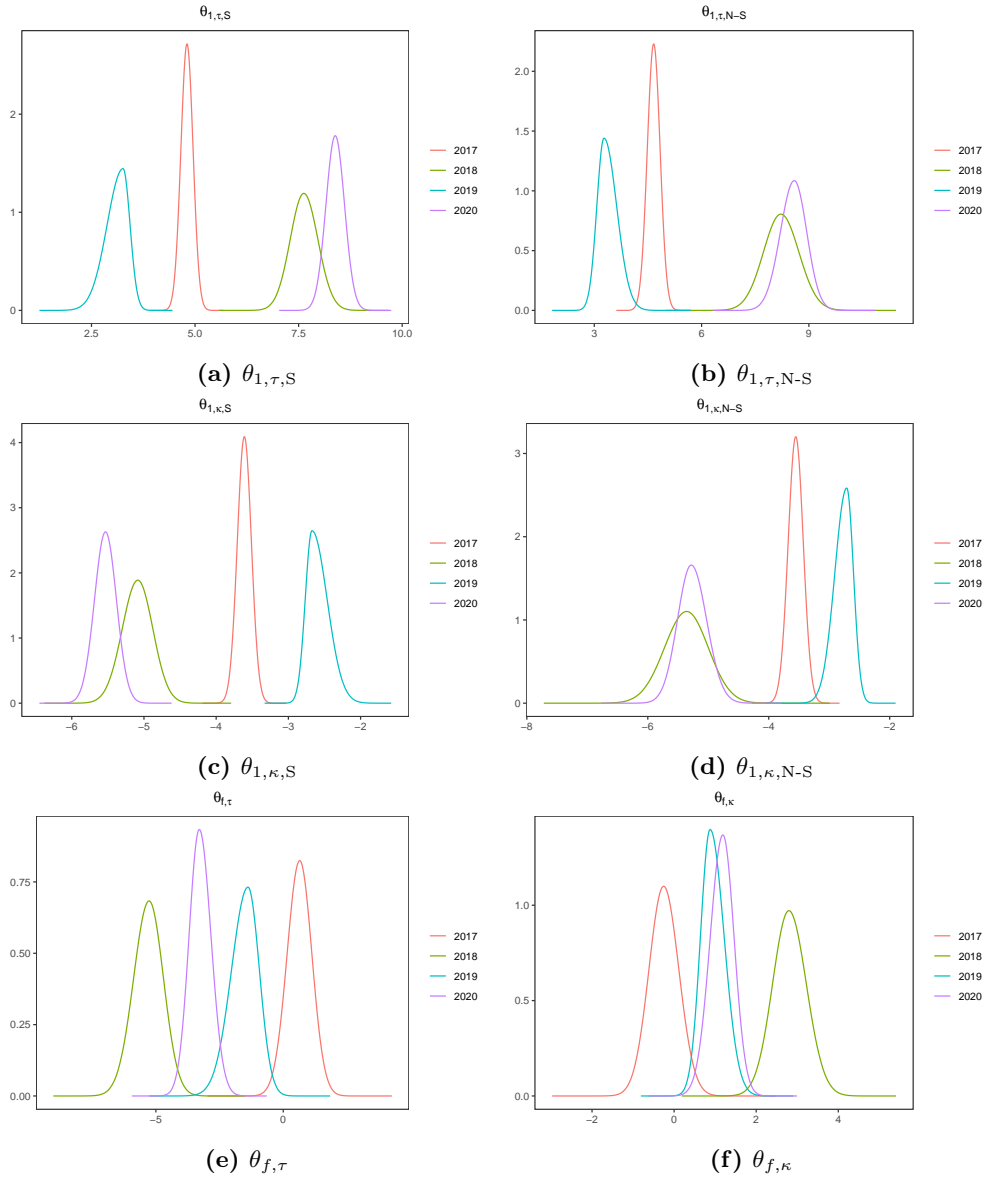where $\Phi(\cdot)$ is the cumulative density function of a Normal(x^*, σ^{2*}) distribution.

Appendix B

Additional results from rutting case study and priors

B.1 Model I fitted to single years

Table B.1: Marginal posterior distributions for the model parameters when fitting Model I_S and $I_{N\text{-}S}$ to the rutting for every single year 2017-2020, one year at a time.

	Model	2017 I_S	2017 $I_{N\text{-}S}$	2018 I_S	2018 $I_{N\text{-}S}$	2019 I_S	2019 $I_{N\text{-}S}$	2020 I_S	2020 $I_{N\text{-}S}$
β		1.18	1.14	0.96	1.04	1.76	1.79	0.84	0.75
$\theta_{1,\tau}$		4.80	4.66	7.63	8.23	3.09	3.39	8.38	8.56
$\theta_{1,\kappa}$		-3.61	-3.55	-5.09	-5.36	-2.58	-2.78	-5.53	-5.26
$\theta_{f,\tau}$			0.63		-5.30		-1.54		-3.25
$\theta_{f,\kappa}$			-0.25		2.82		0.96		1.16
τ_ϵ		2.17	2.18	1.73	2.08	1.45	1.46	1.79	1.93

(a) $\theta_{1,\tau,\mathrm{S}}$

(b) $\theta_{1,\tau,\mathrm{N\text{-}S}}$

(c) $\theta_{1,\kappa,\mathrm{S}}$

(d) $\theta_{1,\kappa,\mathrm{N\text{-}S}}$

(e) $\theta_{f,\tau}$

(f) $\theta_{f,\kappa}$

Figure B.1: Marginal posterior distributions for the SPDE parameters when fitting Model I_S and $\mathrm{I}_{\mathrm{N\text{-}S}}$ to the rutting for every single year 2017-2020, one year at a time.

B.2 Priors in prior sensitivity analysis

Table B.2: Prior distributions for the SPDE parameters in the three prior designs of the prior sensitivity analysis for Model $I_{N\text{-}S}$ for rutting.

	A	B	C
$\theta_{1,\tau}$	$\mathcal{N}(0,10)$	$\mathcal{N}(7.00,10)$	$\mathcal{N}(4.57,0.51)$
$\theta_{1,\kappa}$	$\mathcal{N}(0,10)$	$\mathcal{N}(-4.69,10)$	$\mathcal{N}(-4.75,1.06)$
$\theta_{f,\tau}$	$\mathcal{N}(0,2)$	$\mathcal{N}(-0.23,2)$	$\mathcal{N}(0,1.47)$
$\theta_{f,\kappa}$	$\mathcal{N}(0,2)$	$\mathcal{N}(-0.10,2)$	$\mathcal{N}(0,2.93)$

Table B.3: Prior distributions for the SPDE parameters in the three prior designs of the prior sensitivity analysis for Model $II_{N\text{-}S}$ for rutting.

|	A	B	C
$\theta_{1,\tau,\xi}$	$\mathcal{N}(0,2.5)$	$\mathcal{N}(7.10,2.5)$	$\mathcal{N}(4.57,0.51)$
$\theta_{1,\kappa,\xi}$	$\mathcal{N}(0,2.5)$	$\mathcal{N}(-4.87,2.5)$	$\mathcal{N}(-4.75,1.06)$
$\theta_{f,\tau,\xi}$	$\mathcal{N}(0,2)$	$\mathcal{N}(-4.69,2)$	$\mathcal{N}(0,1.47)$
$\theta_{f,\kappa,\xi}$	$\mathcal{N}(0,2)$	$\mathcal{N}(-2.78,2)$	$\mathcal{N}(0,2.93)$
$\theta_{1,\tau,\omega}$	$\mathcal{N}(0,2.5)$	$\mathcal{N}(10.00,2.5)$	$\mathcal{N}(4.57,0.51)$
$\theta_{1,\kappa,\omega}$	$\mathcal{N}(0,2.5)$	$\mathcal{N}(-6.23,2.5)$	$\mathcal{N}(-4.75,1.06)$
$\theta_{f,\tau,\omega}$	$\mathcal{N}(0,2)$	$\mathcal{N}(-0.50,2)$	$\mathcal{N}(0,1.47)$
$\theta_{f,\kappa,\omega}$	$\mathcal{N}(0,2)$	$\mathcal{N}(-0.25,2)$	$\mathcal{N}(0,2.93)$

Appendix C

Results from simulation study on accidents

Table C.1: Credible interval coverage for parameters from fitting Model I_S and $I_{N\text{-}S}$ to accidents simulated from a stationary and non-stationary GRF $\xi(s)$.

Data	stationary		non-stationary	
	S	N-S	S	N-S
β	0.82	0.81	0.77	0.79
$\theta_{1,\tau}$	0.04	0.00	0.06	0.00
$\theta_{1,\kappa}$	0.00	0.00	0.00	0.00
$\theta_{c,\tau}$		0.73		0.00
$\theta_{c,\kappa}$		0.19		0.06

(a) Stationary data

(b) Non-stationary data
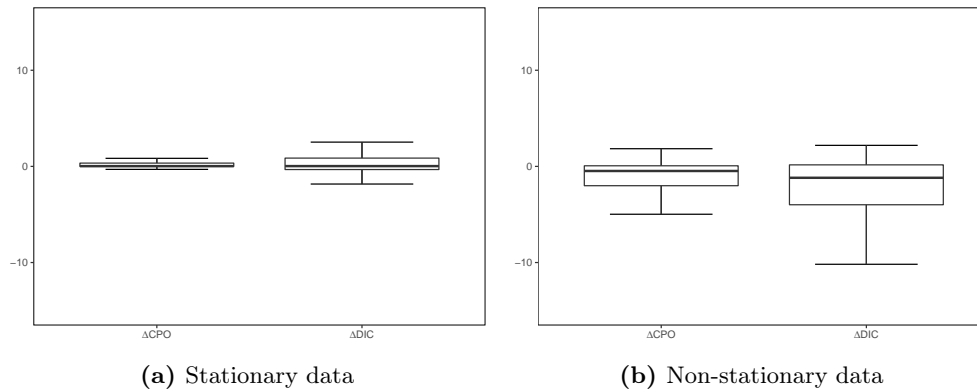
Figure C.1: Difference in CPO and DIC between Model $I_{N\text{-}S}$ and I_S fitted to accidents simulated from a stationary and non-stationary GRF $\xi(s)$.

(a) Stationary data   **(b)** Non-stationary data
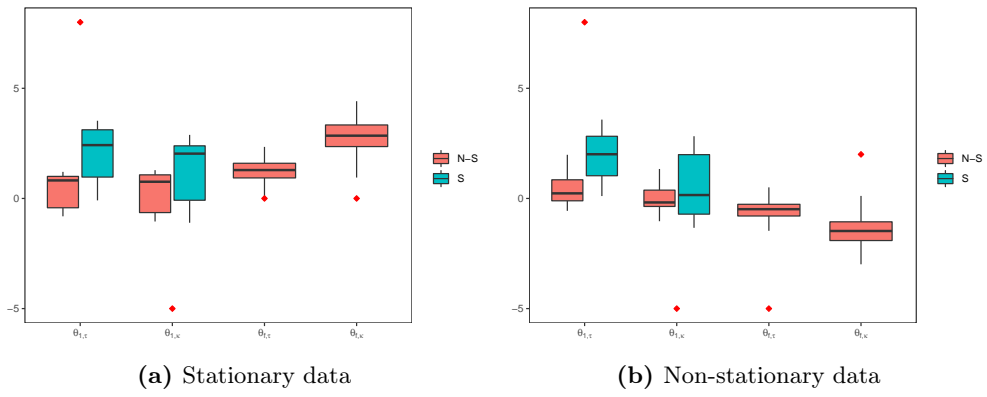
Figure C.2: Boxplot of marginal posterior means for parameters of Model I_S and $I_{N\text{-}S}$ fitted to accidents simulated from a stationary and non-stationary GRF $\xi(s)$. With the true parameter values of the simulated data given by red dots.

Appendix D

Implementation in `R-INLA`

We show code examples for how some of the proposed models for rutting are implemented in `R-INLA`, namely how to generate samples from the spatial field $\xi_{\text{N-S}}(s)$ used in the simulation study in Section 5.2, and the setup and fitting of Model $\text{II}_{\text{N-S}}$ to rutting.

D.1   Simulating from non-stationary GRF

The vector `knots.loc` contains the locations of the vertices for the triangulation, as described in Section 4.1.1, one every 60 meter. The vector `obs.loc` is the observation locations, that is the midpoint for every road segment every year, and `AADT` the traffic intensity at the edges in the triangulation, chosen to be the traffic intensity of the road segment halfway between two vertices, scaled according to the description in Section 4.1.1.

```
# Fix parameter values for simulating from non-stationary Model I
b.0 <- 1.24
theta.tau.1 <- 6.63
theta.tau.f <- -3.27
theta.k.1 <- -4.53
theta.k.f <- 4
prec.err <- 1.58

# Prior means and variances
mu.tau.1 <- 4.57
mu.k.1 <- -4.75

sigma2.tau.1 <- 1.06
sigma2.k.1 <- 0.51
sigma2.tau.f <- 1.47
sigma2.k.f <- 2.93

repls <- 4
n.obs <- length(obs.loc)

# Set up mesh and projection matrix for simulation
mesh1d <- inla.mesh.1d(
  knots.loc,
  interval = c(min(knots.loc) - 500, max(knots.loc) + 500))
```

71

```r
A <- inla.spde.make.A(
  mesh1d,
  loc = obs.loc,
  index = rep(1:n.segs, times = repls),
  repl = rep(1:repls, each = length(unique(obs.loc))),
  n.repl = repls
)


# SPDE
spde.xi <- inla.spde2.matern(
  mesh1d,
  B.tau = cbind(0, 1, AADT, 0, 0),
  B.kappa = cbind(0, 0, 0, 1, AADT),
  theta.prior.mean = c(mu.tau.1, 0, mu.k.1, 0),
  theta.prior.prec = c(
    1 / sigma2.tau.1,
    1 / sigma2.tau.f,
    1 / sigma2.k.1,
    1 / sigma2.k.f),
  alpha = 2
)

# Precision matrix for the Gaussian weights
Q.xi <- inla.spde2.precision(
  spde = spde.xi,
  theta = c(
    theta.tau.1, theta.tau.f,
    theta.k.1, theta.k.f
  )
)

# Generate rutting sample from
# the non-stationary GRF and measurement errors
samp.xi.field <- as.vector(inla.qsample(n = repls, Q = Q.xi))
y.samp <- b.0 + as.vector(A %*% samp.xi.field) +
    rnorm(n = n.obs, mean = 0, sd = sqrt(1 / prec.err))
```

D.2   Fitting non-stationary Model II

The setup for the GRF $\xi_{\text{N-S}}(s)$ in the previous section are used, and we set up the necessary structure for including $\omega_{\text{N-S}}(s)$ and fit Model II$_{\text{N-S}}$. The vector `rut`, contains the rutting for all road segments in the whole period 2017-2020.

```r
# Mesh and projector matrix for pavement stress field omega(s)
mesh1d.omega <- mesh1d
A.omega <- inla.spde.make.A(
  mesh1d.omega,
  loc = obs.loc,
  index = rep(1:n.segs, times=repls)
)

# SPDE for pavement stress, same priors for both GRFs
spde.omega <- spde.xi

# Make indexes for the GRFs
omega.idx <- inla.spde.make.index(
  name = "pavement.field",
  n.spde = spde.omega$n.spde
)

xi.idx <- inla.spde.make.index(
  name = "spatial.field",
  n.spde = spde.xi$n.spde,
  n.repl=repls,
)

# Make INLA stack
stk <- inla.stack(
  data = list(rut = rut),
  A = list(A, A.omega),
  effects = list(c(
    xi.idx,
    list(intercept = 1)
  ), c(omega.idx)),
  tag = "est"
)

# Formula
f.mod2.ns <- rut ~ -1 + intercept +
  f(spatial.field,
    model = spde.xi,
    replicate = spatial.field.repl) +
  f(pavement.field, model = spde.omega)

# Fit non-stationary Model II
mod2.ns.rut <- inla(
  f.mod2.ns,
  family="Gaussian",
  data = inla.stack.data(stk),
  control.family = list(link="identity"),
  control.inla = list(tolerance = 0.000001, h = 0.001),
  control.predictor = list(A = inla.stack.A(stk), compute = FALSE),
  control.compute = list(dic = TRUE, cpo=TRUE)
)
```